Spring 2013

ENSO Effects on Land Surface-Biosphere-Atmosphere Interactions: A Global Study from Satellite Remote Sensing and NCEP/NCAR Reanalysis Data

Henry Bartholomew
San Jose State University

ENSO EFFECTS ON LAND SURFACE-BIOSPHERE-ATMOSPHERE INTERACTIONS: A GLOBAL STUDY FROM SATELLITE REMOTE SENSING AND NCEP/NCAR REANALYSIS DATA

A Thesis

Presented To

The Faculty of the Department of Meteorology and Climate Science

San José State University

In Partial Fulfillment

of the Requirements for the Degree

Masters of Science

by

Henry D. Bartholomew

May 2013

The Designated Thesis Committee Approves the Thesis Titled

ENSO EFFECTS ON LAND SURFACE-BIOSPHERE-ATMOSPHERE INTERACTIONS: A GLOBAL STUDY FROM SATELLITE REMOTE SENSING AND NCEP/NCAR REANALYSIS DATA

by

Henry D. Bartholomew

APPROVED FOR THE DEPARTMENT OF METEORLOGY AND CLIMATE SCIENCE

SAN JOSÉ STATE UNIVERSITY

May 2013

Dr. Menglin S. Jin	Department of Meteorology and Climate Science
Dr. Martin J. Leach	Department of Meteorology and Climate Science
Dr. Eugene C. Cordero	Department of Meteorology and Climate Science

ABSTRACT

ENSO EFFECTS ON LAND SURFACE-BIOSPHERE-ATMOSPHERE INTERACTIONS: A GLOBAL STUDY FROM SATELLITE REMOTE SENSING AND NCEP/NCAR REANALYSIS DATA

by Henry D. Bartholomew

Two mechanisms are examined to reveal the impact of El Niño-Southern Oscillation (ENSO) on land surface, biosphere, and atmosphere interactions. One mechanism is large-scale dynamics—namely, changes in circulation patterns and the jet stream. Another mechanism is local land cover effects, in particular, vegetation and skin temperature. Non-lag and lag correlation coefficients between Niño 3 indices derived from sea-surface temperature (SST) anomalies and land surface variables from satellite based moderate resolution imaging spectroradiometer (MODIS) data, as well as National Center for Environmental Prediction/National Center for Atmospheric Research (NCEP/NCAR) Reanalysis data are analyzed for 2001–2010.

Strong positive correlations between January Niño 3 indices and both air temperature (T_{air}) and skin temperature (T_{skin}) occur over the northwest United States, western Canada, and southern Alaska, suggesting that an El Niño event is associated with warmer winter temperatures over these regions, consistent with previous studies. In addition, strong negative correlations exist over central and northern Europe in January, meaning colder than normal winters, with positive correlations over central Siberia meaning warmer than normal winters.

Despite the different physical meanings between T_{air} and T_{skin}, the general response to ENSO is the same. Furthermore, satellite observations of T_{skin} provide more rich information and higher spatial resolution than NCEP/NCAR Reanalysis data.

ACKNOWLEDGEMENTS

It has been an honor and blessing to have the support of so many great individuals who helped me complete my thesis. First, I want to thank my advisor and mentor, Dr. Menglin Jin. Words cannot describe how much I have learned and how I've been rewarded as a research assistant under her advising. Dr. Jin was always available to help me if I got stuck, and constantly provided feedback on my work so that I could improve and do better next time. I also thank the other members of my committee: Dr. Martin Leach and Dr. Eugene Cordero.

I would like to thank my close friends Terrence Mullens, Colin McKellar, and Amanuel Ghebreegziabher. They were always more than willing to help me if I needed assistance, and constantly created a positive environment both at school and home. There are many other friends I would acknowledge to if I had space, but they know who they are.

Finally, most of all I want to thank my God, who has given me the strength and ability necessary to complete my master's thesis. Without Him, it wouldn't have been possible to do so.

TABLE OF CONTENTS

LIST OF FIGURES

1. Introduction

El Niño is a tropical ocean phenomenon associated with abnormally warm water in the equatorial eastern Pacific region from the coast of Peru to the International Date Line (Namias 1976). It typically lasts between 12 to 18 months and occurs every 3 to 7 years (Wrytki 1975; McPhaden 2002). It develops when the normally predominant northeast trade winds relax, allowing warmer water in the western Pacific to spill back to the east. A La Niña event occurs when the northeast trade winds strengthen, which produces cooler water in the eastern Pacific. El Niño is part of an ongoing feedback loop between the atmosphere and ocean (Rassmussen et al. 1993); the warming of eastern Pacific sea-surface temperature (SST) anomalies off the coast of Peru drives increased convection that increases atmospheric latent heat, further affecting atmospheric circulation anomalies. The greater convection produces westerly wind anomalies at the equator, affecting ocean circulation and helping transport warmer water eastward from the western and central Pacific. In addition, due to modifications in central Pacific surface wind anomalies, upwelling over the eastern Pacific decreases, warming the upper layer of the ocean, and further increasing SST anomalies, starting the cycle over again.

The Southern Oscillation (SO), the atmospheric component of El Niño, is an oscillation of the atmospheric pressure between the western and eastern Pacific. It is measured by taking the difference between the sea-level pressure at Tahiti, French Polynesia and Darwin, Australia (Trenberth 1984). Negative values of SO correspond to warmer SST anomalies, whereas positive values represent cooler SST anomalies (Trenberth and Hoar 1996a).

In the past, there has been confusion over what comprises an El Niño event and how large of an ocean area it covers (Trenberth 1997). Kiladis and van Loon (1988) defined an El Niño event based on a combination of the Southern Oscillation Index (SOI) and eastern tropical Pacific SST anomalies for 160°W to the South American coast and 4°S to 4°N latitude. The requirements for an El Niño event under their definition were a positive SST anomaly of 0.5°C for a minimum of three seasons and a negative SOI below -1.0 over the same period. Nevertheless, newer research suggests that the important region of atmospheric-oceanic interactions in El Niño is located farther west than originally thought (Trenberth and Hoar 1996a), which led to a new index, called Niño 3.5 (Trenberth and Hoar 1996b), extending from 180° to 120°W longitude and 10°S to 5°N. In addition, Trenberth and Hoar (1996b) proposed that events be defined by a positive SST anomaly of at least 0.3°C, rather than 0.5°C. In 1996, the Climate Prediction Center (CPC) established a new index farther west as well, known as Niño 3.4 (Trenberth 1997), which covers an area from 170°W to 120°W longitude and 5°S to 5°N latitude, including most but not all of the Niño 3.5 region, with less latitudinal extent south of the equator. Despite the differences in classification, most studies have generally examined eastern Pacific oceanic SST anomalies in the Niño 3 region (Trenberth 1997), extending from 150°W to 90°W longitude and 5°S to 5°N latitude (Figure 1). This area will be focused on henceforth.

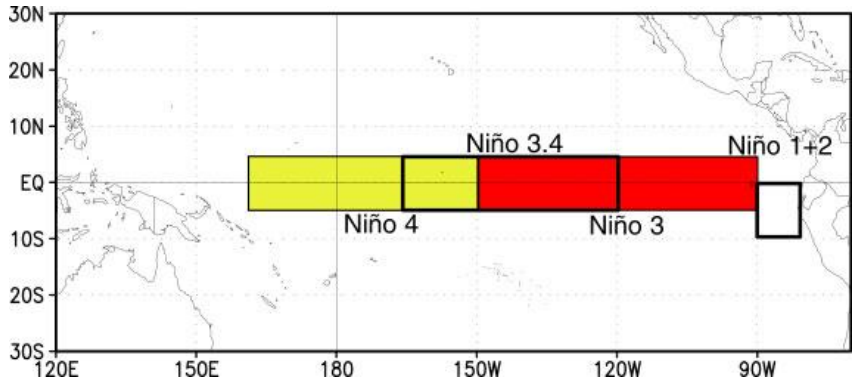

Figure 1: Map of geographic regions of Niño 1+ 2, 3, and 3.4 SST anomalies.

Previous research (Rasmusson and Carpenter 1982; Trenberth 1997) has shown that El Niño tends to develop between the Northern Hemisphere spring and summer months, peaks in the winter months, and usually ends in the following spring. There have been four recent El Niño phenomena since 2000: 2002–2003, 2006–2007, and 2009–2010 (Figure 2).

The coupled atmospheric and oceanic components are referred to as the El Niño Southern Oscillation (ENSO). Although a tropical event, ENSO can affect weather patterns in the mid-latitudes through wavelike patterns that change the jet stream and have a large effect on temperatures (Hurrell 1996), and also affects mid-latitude atmospheric circulation (Namias 1963; Bjerknes 1966, 1969). Tropical forcing of El Niño SST anomalies generates atmospheric response through the fundamental method of Rossby wave propogation (Hoskins et al. 1977; Horel and Wallace 1981; Hoskins and Karoly 1981; Wallace and Gutzler 1981). Additional responses are the result of two other basic methods: the normal-mode instability of zonally varying climatological mean flow (Simmons et al. 1983) and the influence of midlatitude transient eddies associated with storm tracks (Kok and Opsteegh 1985; Held et al. 1989; Hoerling and Ting 1994).

Nevertheless, changes in tropical atmospheric temperatures have been found to occur one to two seasons after initial variations in ENSO (Newell and Weare 1976; Angell 1981; Pan and Oort 1983; Reid et al. 1989; Yulaeva and Wallace 1994; Kumar and Hoerling 2003). However, the time lag between changes varies depending on the region. For instance, higher SST anomalies cause increased convection and thunderstorms in their region (Rassmussen 1993); however, through and after an El Niño event, the global air temperature response usually lags by approximately six months with an observed increase of 0.1°C (Newell and Weare, 1976; Pan and Oort, 1983). Both instantaneous correlations and lag correlations are examined in this study.

Atmospheric responses to ENSO events lead to change in land surface parameters. Jin and Dickinson (2010) suggest that there are two key mechanisms for changes in land surface parameters: large-scale dynamics and local effects. Large-scale dynamics are the physical processes over large-scale areas that lead to displacement of clouds, rainfall, solar radiation, and circulation patterns. Local effects, on the other hand, are local land use and land cover influences such as urbanization, deforestation, and vegetation change. For example, temperature responses in a large city caused by an El Niño event could be different from changes in a rural area (Jin and Shepard 2008). Using a fine-mesh land model, Hahmann and Dickinson (2001) found that tropical precipitation and mid-latitude surface temperatures are sensitive to changes in land cover. Deforestation can actually lead to increased ENSO variability (Schneider et al. 2006), as well as a weakening of the Walker-Hadley circulation (Zeng et al. 1996). Thus, deforestation can influence the temperature effects due to El Niño. Deforestation also

increases the greenhouse effect and could lead to large-scale climatic effects (Shem and Dickinson 2006).

Two major features are reported for the ENSO effect on North America. One is cooler winter conditions in the gulf states including Florida (Ropeleski and Halpert 1986; Wang and Fu 2000) due to a stronger influence of the subtropical jet stream. Although overall temperatures are slightly cooler because more cloudy and rainy days result due to less solar insulation at the surface, the number of extreme cold spells and frosts actually decreases. This is due to less penetration of strong polar jet stream troughs over the region because of the dominating subtropical jet (FCC 2009). During an El Niño, there is greater probability of a positive Pacific-North American teleconnection pattern (PNA) (Yarnal and Diaz 1986) associated with below normal height anomalies over the southeast United States (Kumar and Hoerling 2003), which helps explain the above pattern. Additionally, in this region the ENSO signal has been found to be the strongest during fall and winter (Ropelewski and Halpert 1986; Sittel 1994a, 1994b).

The second feature is that warmer winters are present over the West Coast, in Alaska, and over Southern Canada (Kiladis and Diaz 1989) with lower precipitation amounts in the northwest United States (Ropelewski and Halpert 1986) due to the PNA (Horel and Wallace 1981; Ropelewski and Halpert 1986). A positive PNA is correlated with an upper level ridge of high pressure over the West Coast. This helps explain warming over the region. Furthermore, as a result of an increased southerly flow and a deeper Aleutian low, the teleconnetions lead to widespread warming in Alaska and western Canada (Trenberth 1997). On the contrary, a La Niña event is usually associated

with cooler and wetter winter conditions over the northwest United States extending into Canada and southern Alaska. Therefore, strong positive correlations between Niño 3 indices and temperatures are expected over these regions, which are proven in our study using high resolution satellite observations.

The effects of El Niño on Europe are not as clearly known as those on regions including North America and Australia (Ricard 2000). Despite the long spatial distance from the eastern Pacific Ocean to Europe, atmospheric teleconnections can be identified (Wilby 1993; Fraedrich 1994), although not as clearly as for the North American region. Studies of the temperature effects on the region, however, have produced conflicting results. Fraedrich (1994) found that El Niño results in colder wintertime weather over central and northern Europe. However, Hurrell (1996) found that SO negative deviations that correspond to warmer eastern Pacific SST anomalies, are associated with warmer January temperatures throughout Siberia and Eastern Europe, with very little change over western and northern Europe. Using the most advanced satellite data, our results support the findings of the association of ENSO, with cooling over central and northern Europe (Fraedrich 1994) and warming over eastern Europe and Siberia (Hurrell 1996).

The unique approach of this study is the use of satellite skin temperature measurements that provide more information than air temperature. Skin temperature (T_{skin}), also known as "radiometric surface temperature" (Jin et al. 1997), can be retrieved through satellite observed upward longwave radiation emitted by the Earth's surface. The inverse of Planck's Law can be used to convert this upward radiant flux to T_{skin}. Under clear sky conditions, algorithms have an accuracy of 0.5–1.0°C (Coll et al. 1994;

Becker and Li 1995; Wan and Dozier 1996). While surface temperature is usually defined as the air temperature at two meters above the ground (T_{air}), T_{skin} is considered more representative of the temperature of the actual earth's surface (Jin and Dickinson 1999; Jin and Mullens 2012). It has a different physical meaning from surface temperature, as well as a larger diurnal range (Jin and Dickinson 2010).

ENSO is a very important phenomenon, and the goal of this study is to examine its relationships to various satellite-measured land surface parameters. Section 2 examines the methodology and data used for this project. Section 3 presents the ENSO relations with T_{skin} and T_{air}. Uncertainty analysis is presented in Section 4. Section 5 outlines the main conclusions. Finally, Section 6 highlights future work.

2. Data and Methods

Monthly Niño 3 SST indices, calculated by computing the Empirical Orthogonal Function (EOF) on Niño 3 SSTs to represent a perturbation from the average, were obtained from the CPC website (http://www.cpc.ncep.noaa.gov/data/indices/sstoi.indices). Each value represents an average anomaly over the Eastern Pacific tropical region between 5°S–5°N and 150°W–90°W. These data were correlated with Moderate Resolution Imaging Spectroradiometer (MODIS) data for the same period, as well as National Center for Environmental Prediction/National Center for Atmospheric Research (NCEP/NCAR) reanalysis data.

MODIS is flown on two NASA polar orbiting satellites: Aqua and Terra, with each having its own advantages and disadvantages. Terra data were examined in this study as it has a longer temporal period, with data being available from March 2000 to the present, as opposed to Aqua, which only has data available starting in August 2002 (Schaaf et al. 2002; Jin and Mullens 2012). Terra flies north-south over the daytime side of the earth, reaches the polar regions, and flies south over the nighttime side. This allows measurements to be made over a point twice daily: at 10:30 a.m. (daytime, also called ascending) and 10:30 p.m. (nighttime, also called descending) local time.

Three MODIS measurements monthly mean land surface parameters were examined: daytime skin temperature (T_{skin}), daily normalized difference vegetation index (NDVI), and daily column precipitable water vapor (PWV). Daytime T_{skin} data are part of the MOD11C2 product, with a resolution of 0.05° latitude x 0.05° longitude (Wan 2007). This corresponds to 720 x 360 = 259,200 grid points globally. NDVI is a

measure of the amount of greenness of a surface and ranges in value from – 1 to 1. The negative values on the scale correspond to water, whereas values close to 0 indicate barren areas, such as desert sand or rocks. Grassy and shrubby areas are represented by low positive values, whereas those close to 1 represent forests. NDVI has the same resolution as T_{skin}, and the data are part of the MOD13C2 product suite. PWV data has a lower resolution of 1° x 1°, and is part of the MOD08 product suite. It represents the total amount of water vapor in a column, and is derived over land during daytime through the use of a near-infrared algorithm (King et al. 2003).

NCEP/NCAR reanalysis data is available from 1948 to the present. Monthly data were examined over the period between 2001 and 2010 for two variables: land surface or skin temperature (T_{skin}) and air temperature (T_{air}). The resolution is 2.5° x 2.5° for T_{air} temperature, but variable for T_{skin}. There are 192 (latitude) x 94 (longitude) = 18,048 grid points for land surface temperature, ranging from 88.542°S to 88.542°N latitude and 180°W to 180°E longitude. The grid spacing is approximate 1.9° for latitude (varies slightly by less than 0.1°) and exactly 1.875° for longitude. To generate a correlation on a global scale, each month's MODIS T_{skin} data array, which has 0.05° x 0.05° spatial resolution, was re-gridded to 0.5° x 0.5° resolution using bilinear interpolation.

Pearson Product-Moment correlation coefficients between Niño 3 and T_{skin} over 2001–2010 were then calculated. Each month contained one Niño 3 index, and there were 120 total months of data. On one hand, spatially, Niño 3 data were a one-dimensional function of time. On the other hand, the T_{skin} array was three-dimensional, as it represented a function of latitude, longitude, and time. For 2001–2010, over each

pixel, each January T_{skin} (10 total) was temporally correlated with the corresponding Niño 3 index (10 total). This was done over the entire global grid. Next, the same correlation was done for July, and the same procedure was done for PWV. In addition, temporal correlation coefficients were calculated between NDVI and T_{skin} for January and July of the period. Finally, in order to determine which regions are most sensitive to changes in ENSO, the standard deviation (SD) of yearly correlation coefficients over each pixel was computed.

For each month, while there would be 259,200 total pixels of daytime skin temperature, each of these would be compared with only one Niño 3 value. The correlation was done over all months of a year so that it could be seen how closely the Niño 3 SST anomaly annual cycle was related to that of land surface parameters. Next, temporal correlation coefficients were calculated for all Januarys and all Julys of the period at each pixel for T_{skin} and PWV, and all Februarys and Julys for NDVI. Thus, for January, an array of skin temperatures over 2001–2010 would be correlated with an array of the Niño 3 anomalies, and the coefficient would be produced. The same method applied for the July values. In order to account for time between the development of an El Niño and corresponding atmospheric effects, six-month lag correlation coefficients were calculated as well. Correlation coefficients were calculated over the ten-year period between January and July, and also for July and January of the next year. Finally, SDs of yearly correlation coefficients were computed to determine which regions are most sensitive to changes in ENSO. A similar method was done for the NCEP/NCAR data. Lag correlation coefficients were calculated between the Niño 3 index and NCEP/NCAR

T_{skin} for January through July and July through January, similar to above for MODIS. They were also calculated between Niño 3 and NCEP/NCAR T_{air}.

The analyses each had ten data points (n = 10) which corresponded to eight degrees of freedom (df = n – 2 = 10 – 2 = 8). Using a Pearson Product-Moment Correlation Coefficient table, a level of significance (p) of 0.05 for df = 8 corresponds to a correlation coefficient (r) of 0.632. Thus, to be statistically significant at the 95% confidence interval, r must be greater than or equal to 0.632, or less than or equal to – 0.632. The closer the value of r is to 0, the lower the correlation and greater the chance that the relationship found could be due to pure chance.

3. Results

a. Niño 3 and T_{skin}

Three major El Niño events occurred during the 2001–2010 period: 2002–2003, 2006–2007, and 2009–2010, as evidenced by positive anomalies of Niño 3 indices (Figure 2). Conversely, there were four La Niña events over the period. They were present for 2000–2001, 2005–2006, 2007–2008, and 2010–2011. Thus, even though we only have ten years of MODIS data, there was adequate information about SST anomalies, as there were a total of seven occurrences of either a El Niño or La Niña event during the timeframe.

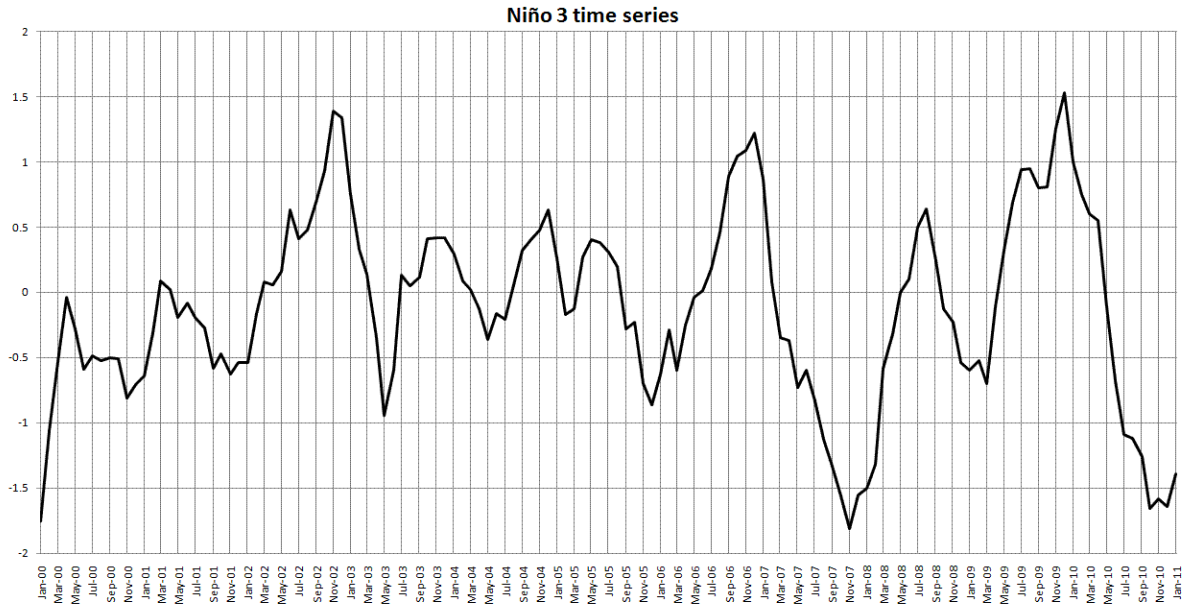

Figure 2: Plot of Niño 3 SST indices with respect to time for 2000 − 2010, calculated by computing Empirical Orthogonal Function (EOF) on Niño 3 SSTs. Data from Climate Prediction Center website (http://www.cpc.ncep.noaa.gov/data/indices/sstoi.indices).

Correlation coefficients of Niño 3 and T_{skin} help to identify those regions T_{skin} is sensitive to ENSO (Figure 3a). Very high positive coefficients suggest that an increase in

January T_{skin} from one year to the next tends to be associated with an increase in the Niño 3 value for the same month. On the contrary, strong negative correlation coefficients suggest that higher Niño 3 SST anomalies are associated with cooler T_{skin} values. The highest values (0.8–1) are found on the Russia-Kazahkstan border northeast of the Caspian Sea, in parts of interior Russia, and in areas along the northern edge of Antarctica. In particular, the maximum is 0.85 on the southwestern edge of the Caspian Sea. The strongest negative value (– 0.82) is located in southwestern Africa at 20°S and 15°E. In North America, there are positive coefficients along the west coast of the United States extending into Canada and Alaska; this agrees with the finding of higher than average temperature anomalies along the West Coast, in Alaska, and over Southern Canada during an El Niño event. (Kiladis and Diaz 1989). In addition, correlation coefficients of 0.2–0.8 are present over the Rocky Mountains. The Great Plains and midwest regions have slight to moderate negative correlation coefficients of 0 to – 0.6. Strong negative correlation coefficients exist over northern Mexico (– 0.4 to – 1), indicating that warmer Niño 3 SST anomalies in January are associated with lower T_{skin} values, while the southeastern Unites States region generally has small negative correlations (0 to – 0.4), although stronger in Florida (up to – 0.6).

In Europe, there are strong negative correlation coefficients (– 0.4 to – 1) over the Northern European region including Denmark, Sweden, and Norway. Eurasia, on the other hand, has slight positive correlations across its interior (0 to 0.4), increasing to higher values in the far eastern portion (0.4 to 0.8). This corresponds with the observation that higher eastern Pacific SSTs are associated with warmer January temperatures in this region (Hurrell 1996).

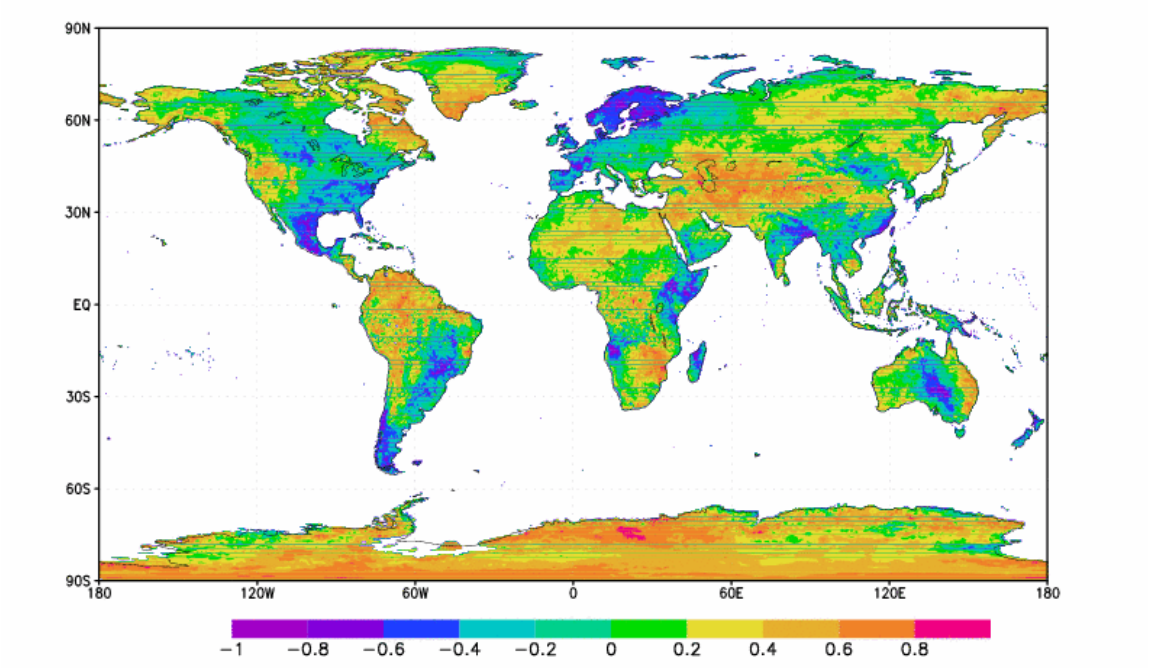

Figure 3a: Correlation coefficients between January Niño 3 SST anomalies and January MODIS Daytime T_{skin} (0.05°x0.05° resolution, regridded to 0.5°x0.5°) over the period of 2001–2010.

Many of the very low values of less than – 0.6 tend to be concentrated along or near the coast of continents as opposed to inland, including southeast Brazil, southern Chile, the southern edge of Saudi Arabia, the eastern tip of Africa, and other areas. A notable exception to this trend occurs in Australia, which has the strongest negative correlations in the interior of the continent.

Furthermore, three major areas have negative correlations over large valleys and flatlands with positive correlations over nearby mountains. In Australia, the central lowlands have negative correlations as low as – 0.6 to – 1, while the Great Dividing Range is associated with positive values. In the United States, the intermountain west generally has positive correlations of 0.2 to 0.8, but there are a few areas with values of 0 to 0.2, including the southern end of the Central Valley of California (between the coast

ranges and Sierra Nevada), and the south end of the Puget Sound and Chehalis Valley in Washington (between the Olympic Mountains and Cascades). Finally, between 30°S and 60°S in South America, there are strong negative correlations along the coast west of the Andes, with positive correlations in some areas of these mountains. These findings raise an interesting question: Is there evidence that higher-than-normal Niño 3 SST anomalies in January are associated with cooler large scale valleys and flatlands worldwide? This could be an example of a local effect of ENSO.

By contrast, in July, Niño 3 SST anomalies and T_{skin} can demonstrate large differences (Figure 3b) from the pattern in January. For example, correlation coefficients over the Norway/Sweden/Finland region are negative and between -0.2 to -1 in January, while in July, they are positive and between 0 and 0.8. In addition, values go from negative (0 to – 0.6) to positive (0 to 0.8) over much of the eastern half of the United States, in particular the Gulf Coast and southern Plains. Furthermore, strong negative correlation coefficients in January over Mexico are now replaced with positive correlations in July. Finally, over the far eastern portion of Eurasia, there is a large shift from moderate to strong positive correlation coefficients in January (0.4 to 0.8) to highly negative coefficients in July (– 0.6 to – 1).

The strongest negative correlation coefficient value for July is – 0.89, found at 45°N and 120°E. The area of negative values in this region generally range from – 0.6 to – 0.8. Large regions of positive correlations are present over an area extending from northern Mexico to the southern Great Plains, the southern portion of South America including Argentina and Chile, and Australia. The pixel with the highest positive

correlation coefficient is located over the southern Sahara Desert, with a value of 0.89. The aforementioned areas of positive correlations are in the subtropical vicinity of 30°N or 30°S. On the other hand, the two areas of strongest negative correlations are centered near 60°N.

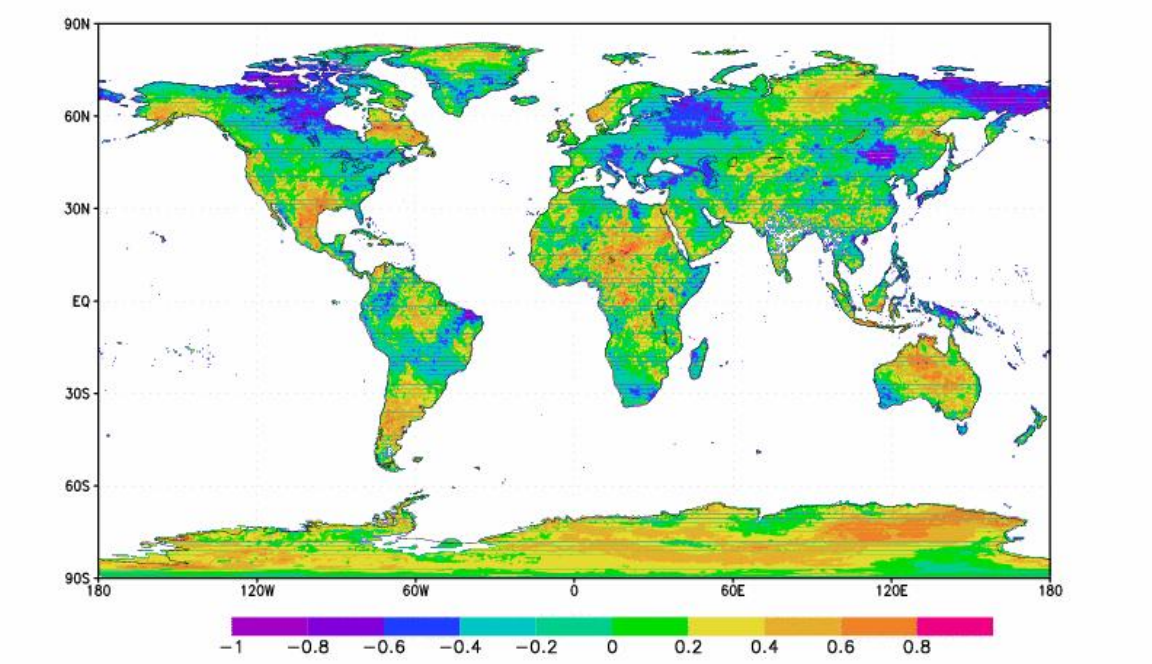

Figure 3b: Correlation coefficients between July Niño 3 SST anomalies and July MODIS Daytime T_{skin} (0.05°x0.05° resolution, regridded to 0.5°x0.5°) over the period of 2001–2010.

In North America, areas of the United States along the west coast and southern Alaska have small to strong positive correlation coefficients (0.2 to 0.8), while most of the northeast is covered by weakly negative correlations (0 to -0.4), although a few stronger spots are present (– 0.4 to – 0.6). Positive correlations cover most of Australia (0.2 to 0.8), with an area of negative values present over the southwestern corner (– 0.2 to – 0.6). Finally, patterns over Europe and Asia are quite variable, with differences as noted.

Lag correlations between January Niño 3 SST anomalies and July T_{skin} (Figure 4a) show that key regions with negative correlation coefficients (– 0.4 to – 0.1) occur over South America in the vicinity of 30°S, a section of the southern and southeastern United States and extreme northern Mexico, and a swath in the northern tropical latitudes of Africa.

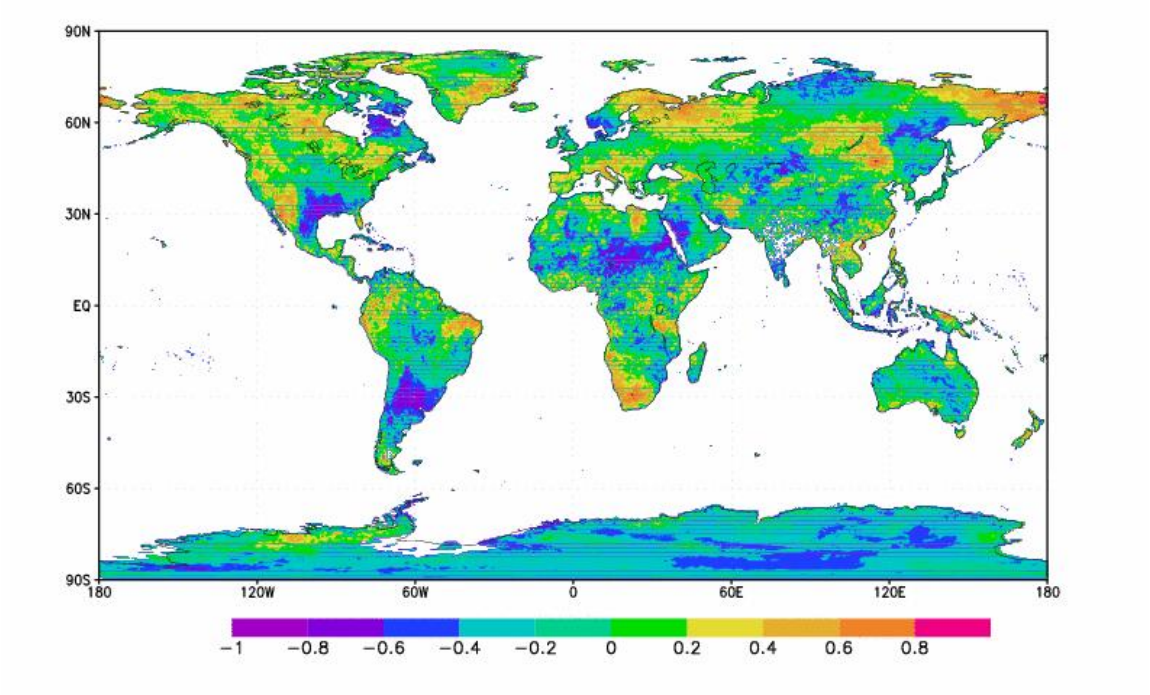

Figure 4a: Lag correlation coefficients between January Niño 3 SST anomalies and July MODIS Daytime T_{skin} (0.05° x 0.05° resolution, regridded to 0.5° x 0.5°) over the period of 2001 – 2010.

In particular, the strongest positive correlation is 0.90 over extreme eastern Siberia (65°N, 175°E) and the strongest negative correlation is – 0.83 (35°S, 75°W). In addition, strong positive correlations (> 0.6) occur over far eastern Siberia, eastern Brazil, part of the southwestern United States, South Africa, and an area near the Russia/China/Mongolia region.

Since T_{skin} represents the surface temperature of the land, it is very sensitive to vegetation type, as governed by the surface energy budget (Jin and Dickinson 2010). A large difference occurs between the southwest and southeast United States partly due to differences in land type and vegetation coverage. Specifically, high positive values occur over desert areas and mixed terrain, while flatter grasslands are present to the east with negative values. This is a good example of the local mechanism influencing the effect of ENSO on T_{skin}. Because T_{skin} represents the surface temperature of the land, it is very sensitive to vegetation type, seen from this example.

Comparing the non-lag correlations of July Niño 3 SST anomalies (Figure 3b) to lag correlations for January and July (Figure 4a) reveals a number of important differences. First, while the non-lag correlation has distinct strong negative correlation in regions at 60°N latitude (90°W, 50°E, and 150°E longitude), the lag correlation has many regions of positive correlations at this latitude. In addition, at 30°N and 30°S, there is evidence of reversal from positive (non-lag) to negative (lag) as well. For example, the northern Mexico and southern United States region at 100°W has strong positive correlations of 0.4 to 0.8 for non-lag July, but negative correlations of – 0.4 to – 0.8 when a lag is performed.

The plot of correlation coefficients between July Niño 3 anomalies and January T_{skin} (Figure 4b) is important to examine, because it shows two critical features. First, it reveals the time interval between SST warming and the corresponding atmospheric response. Second, it may suggest how T_{skin} is affected in Northern Hemisphere winter

when the effects of ENSO are most apparent, as mentioned in the literature (Sittel 1994a, 1994b).

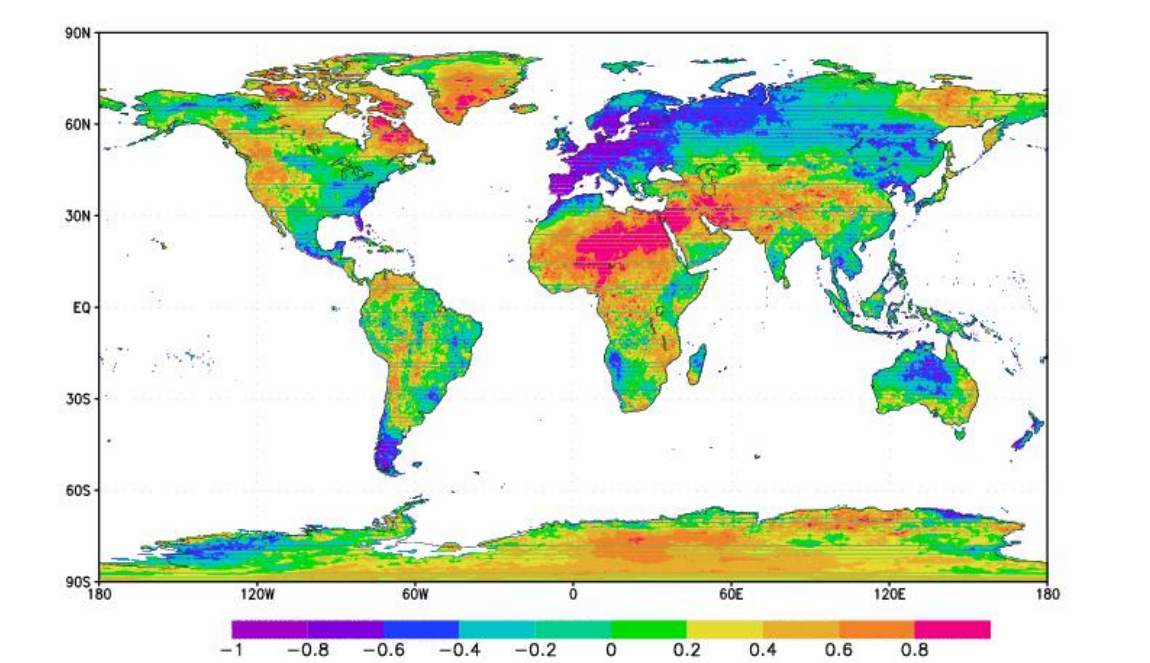

Figure 4b: Lag correlation coefficients between July Niño 3 SST anomalies and January MODIS Daytime T_{skin} (0.05° x 0.05° resolution, regridded to 0.5° x 0.5°) over the period of 2001–2010.

The highest correlation is 0.95 over the Sahara Desert (15°N, 15°E), and the lowest is – 0.93 in eastern Spain (40°N, 10°W). The most distinctive region is the large swath of positive values (0.8 to 0.95) over northern Africa, which suggests a very strong relationship between Niño 3 SST anomalies and T_{skin} over the region. Conversely, very strong negative correlation coefficients are present over western and central Europe, including Portugal, Spain, France, and Germany. This is an important finding because there are still uncertainties about how exactly ENSO affects Europe.

Focusing over North America, high negative values occur over Florida and western Cuba (– 0.6 to – 1), which is consistent with the finding that El Niño conditions

are usually associated with cooler winter conditions over the Gulf States (Ropeleski and Haplert 1986; Wang and Fu 2000). Nevertheless, eastern Cuba correlations are close to 0. In addition, there is a large swath of strong positive correlation coefficients (> 0.6) extending southward from Alaska into British Columbia and the northwestern United States, supporting the finding that an El Niño event usually produces warmer winters over the area (Ropeleski and Haplert 1986; Kiladis and Diaz 1989). Furthermore, it appears that the Appalachian Mountains have stronger negative correlations than the surrounding areas of lower elevation.

To determine which relationships are most meaningful, areas of statistical significance were plotted for the correlations between July Niño 3 SST anomalies and January T_{skin} (Figure 5). Because there are ten data points (n = 10), the degrees of freedom is eight (df = n – 2 = 10 – 2 = 8), and using a Pearson Product Moment Correlation table yields this correlation value for a 95% confidence level. To be statistically significant at a 95% confidence level, the correlation coefficient must be greater than or equal to 0.632, or less than or equal to – 0.632. When examining the areas of statistical significance, major key patterns can be seen. First, the aforementioned areas of negative correlations over western and central Europe are statistically significant at the 95% level, as is the belt of positive correlations extending from northern Africa into the Middle East. There are also areas of significance over the over the parts of the western United States and western Canada. In addition, an interesting wavelike pattern is observed over southern Greenland, while strong cooling occurs over western Europe. This could be related to the jet stream patterns present for an El Niño, that is, a ridge over eastern Canada and southern Greenland, and a trough over western Europe. Although it

might be too optimal to assume that these ten years of data represent a normal independent distribution, which is the key assumption for the Pearson-Product Moment Correlation Coefficient, this statistical analysis sheds inside on possible significance of the ENSO effect.

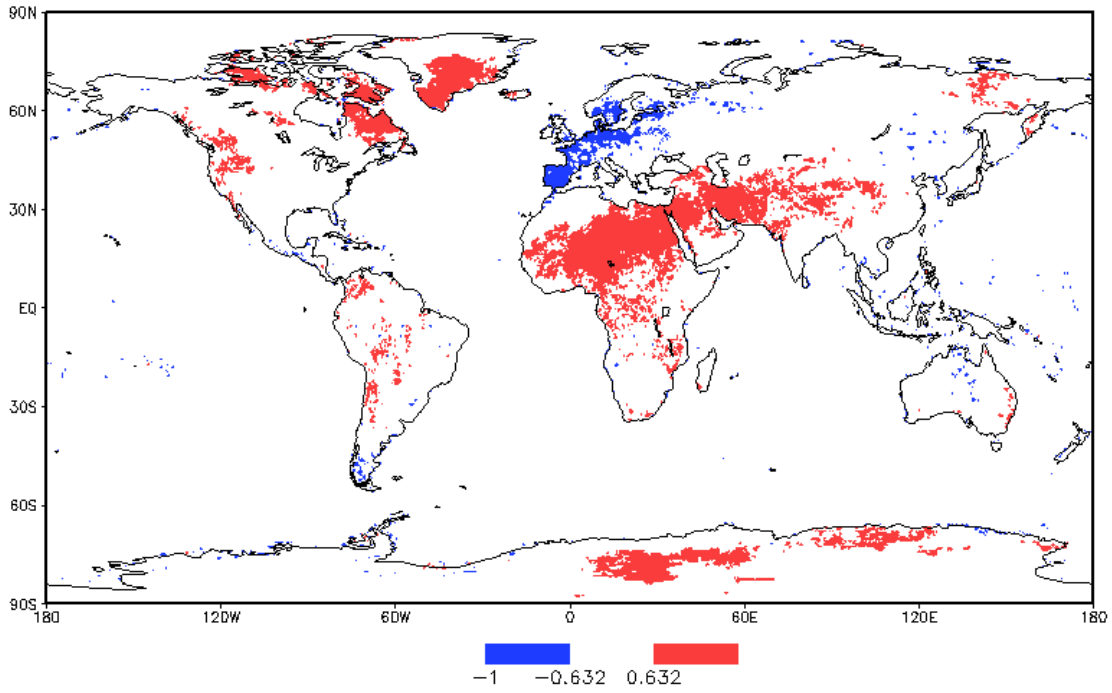

Figure 5: Areas of 95% statistical significance for the lag correlation coefficients between July Niño 3 SST anomalies and January MODIS Daytime T_{skin} over the period of 2001–2010.

To see the relationship of Niño 3 SST anomalies and T_{skin} over a 12-month cycle, correlations were also done on a yearly scale. Specifically, temporal correlation coefficients were calculated between Niño 3 SST anomalies and T_{skin} for each year of the period. A comparison of correlations for individual years shows great variability, from highly negative to highly positive or vice versa. The SD of yearly correlation coefficients over the 2001–2010 timeframe was calculated to test the sensitivity of land regions (Figure 6). Low SDs represent little change in yearly correlation values, while high SDs explain large variations in correlations. The highest SDs are 0.6–0.9 occurring over the

eastern tip of South America in Brazil, much of the southern portion of Africa, and parts of western and northern Australia. Thus, the areas of high variability generally occur in the tropics between 30°N and 30°S, although mostly in the southern hemisphere.

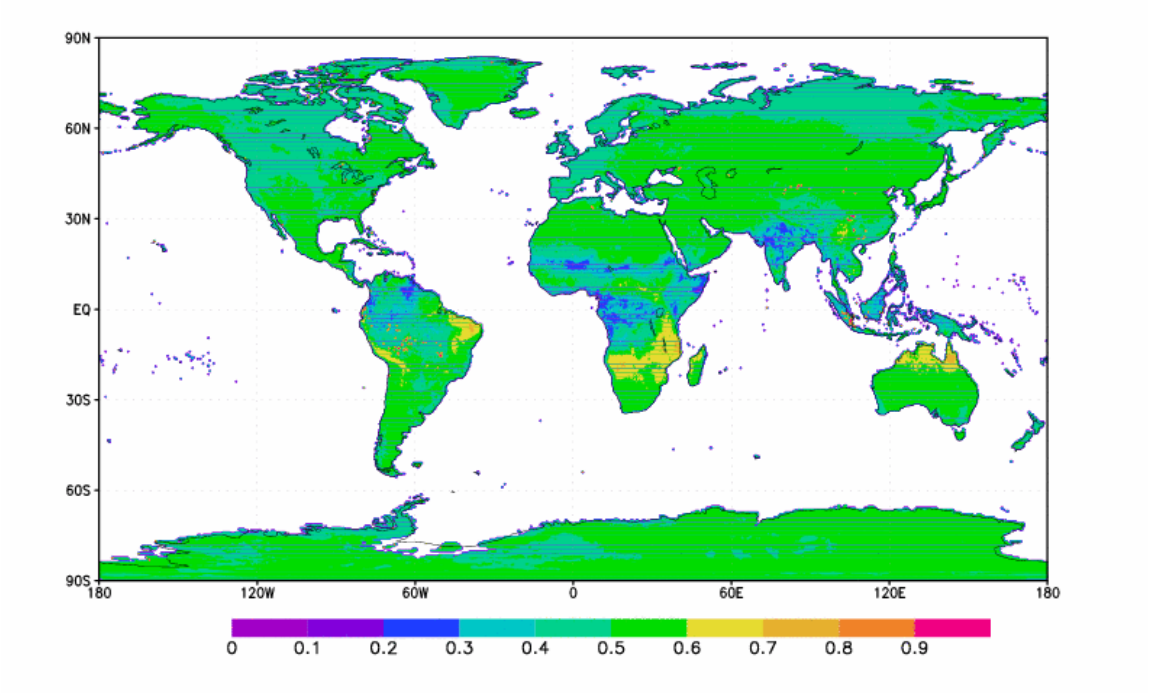

Figure 6: SDs of yearly correlations for Niño 3 SST anomalies and MODIS T_{skin} over the period of 2001–2010.

The lowest SDs of 0.1–0.3 occur in equatorial and sub-tropical regions, including parts of northern South America, central Africa, and much of India. Most areas in the mid-latitudes in the Northern Hemisphere have values of 0.5–0.6. There is clearly more variability in the Southern Hemisphere.

b. Niño 3 and T_{air} vs. T_{skin}

Comparing the lag correlation between January Niño 3 SST anomalies and July NCEP/NCAR T_{skin} (Figure 7a) to that of MODIS, the patterns are similar with differences over Africa and Australia. Notable similarities include the negative correlation regions

over the south and southeast United States and South America, and large areas of positive correlations over northwestern Europe and central and eastern Siberia, with high positive values over Eastern Brazil as well. However, the area of negative correlations in South America is much larger in latitudinal area for the NCEP/NCAR data, extending north to the equator, rather than 30°S for the MODIS data. Nevertheless, values are in the same range (– 0.4 to – 1). The point in eastern Brazil of highest values is shifted west slightly for the NCEP/NCAR data. The large positive region over northwestern Europe and central and eastern Siberia appear very similar in both plots, in both area and detail. With the exception of the area of negative correlations over the south, most of North America varies between very slightly positive (0 to 0.4) to more strongly positive (0.4 to 0.8) using both sources. Despite the lower resolution of NCEP/NCAR, patterns are generally the same. Finally, there are a few small spots of negative correlations in Europe that are similar in location and magnitude: one at about 70°N 90°E, one at 60°N 120°E, and another at 30°N 100°E.

Three major differences are observed. First, while the MODIS correlation shows values close to or at zero over Australia, the NCEP/NCAR plot has a distinct region of positive values at the northern end of this area (0.2–0.8), which is completely absent from the other source. Second, the region of strong positive correlation coefficients over southern Africa from the MODIS data is not present in the NCEP/NCAR plot. Instead, a region of very high correlations is present just to the north. Finally, the belt of very strong negative correlations in northern Africa from the MODIS data is replaced by a swath of the opposite sign.

A discussion of the correlation between July Niño 3 SST anomalies and January T_{skin} from NCEP/NCAR Reanalysis Data (Figure 8a) along with its relationship to the same correlation done using MODIS data (Figure 4b) now follows. The major patterns found are similar in both cases; nevertheless, there are some minor differences.
The major large scale patterns existing for both cases include the region of high positive correlations over the northwest United States extending into Alaska, and very strong negative correlations over northwestern Europe. However, the swath of very high correlations over the Sahara Desert is not quite as strong; only a couple small regions of values > 0.8 are present, with values mostly from 0.4 to 0.8. In Australia, unlike the clear difference that was seen for the January–July correlation, the pattern for July–January is the same, with negative correlations in the northernmost areas of the continent and slightly positive values over the Eastern Highlands.

The correlation between Niño 3 SST anomalies in January and T_{air} from the following July shows remarkably similar patterns to those found for T_{skin} (Figure 7b). Focusing on the large distinctive patterns, the swath of negative correlations in South America appears similar in both size and magnitude, as do the three positive regions over Russia. The spot of negative values over the southeastern United States is similar, and the general pattern of positive values from the northwest United States into Alaska is the same. One difference between the two different types of temperature is that the latitudinal band of positive correlations in northern Africa around 30°N is not as strong when using T_{air}.

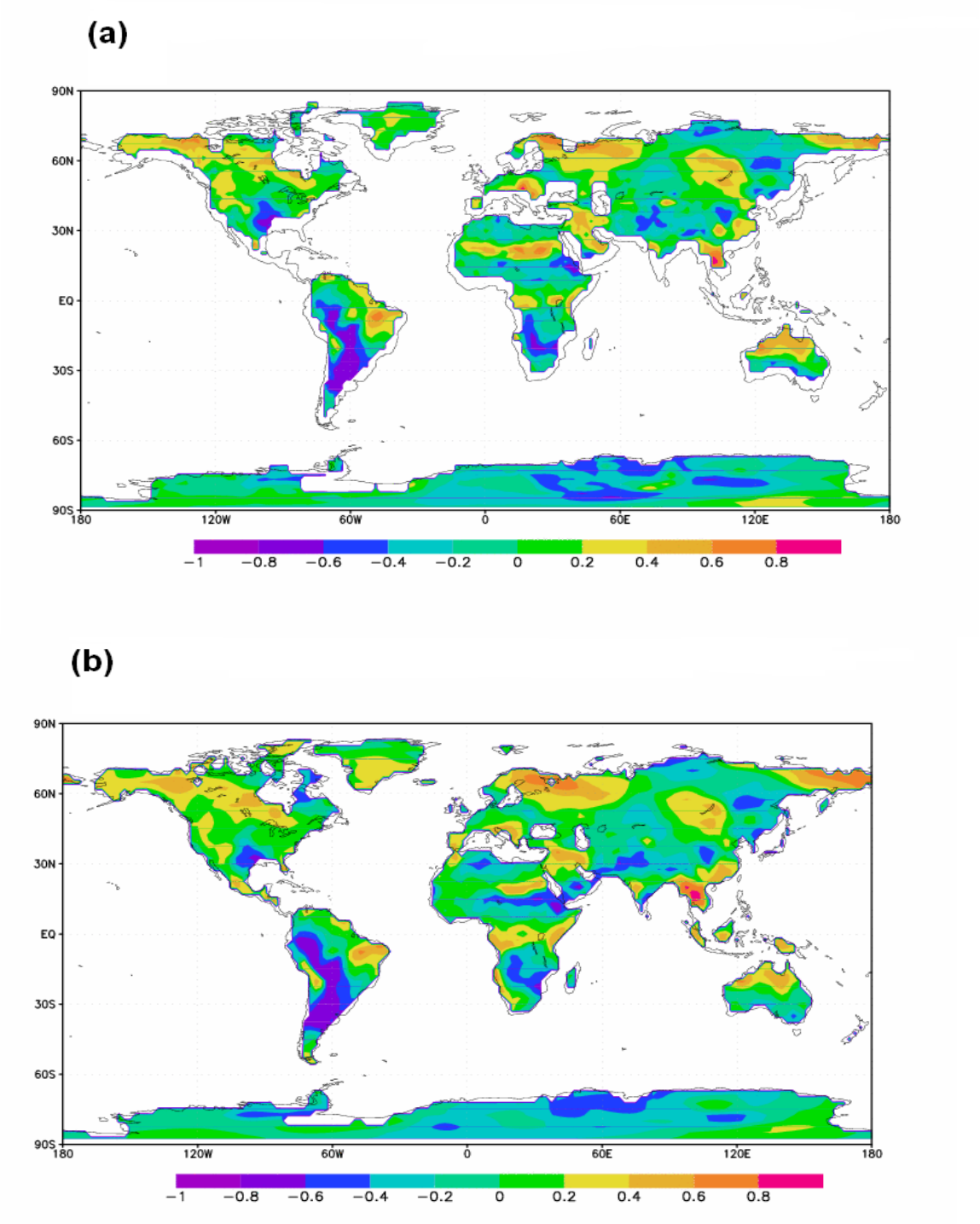

Figure 7: NCEP/NCAR Reanalysis lag correlation coefficients between January Niño 3 SST anomalies and July NCEP/NCAR T_{skin} (192 x 94 grid points) **(a)** + T_{air} (144 x 73 grid points) **(b)** over the period of 2001–2010.

A comparison of the correlations between July Niño 3 SST anomalies and January T_{skin} and T_{air} (Figures 8a, 8b) from NCEP/NCAR reanalysis data now follows. First, one

important difference exists for the swath of positive values over northern Africa. The analysis done using MODIS T_{skin} shows a more significant region than NCEP/NCAR T_{skin}, but the plot using MODIS T_{air} agrees more with NCEP/NCAR T_{skin}. In general, most of the large patterns are similar, such as the regions of positive values over northern South America and the strong negative correlation coefficients over western and central Europe, as well as smaller areas. An important feature is the belt of strongest negative correlations (< -0.6) over northwestern and north-central Europe, and past research has shown a possible wintertime cooling over northern and central Europe for an ENSO event (Fraedrich 1994).

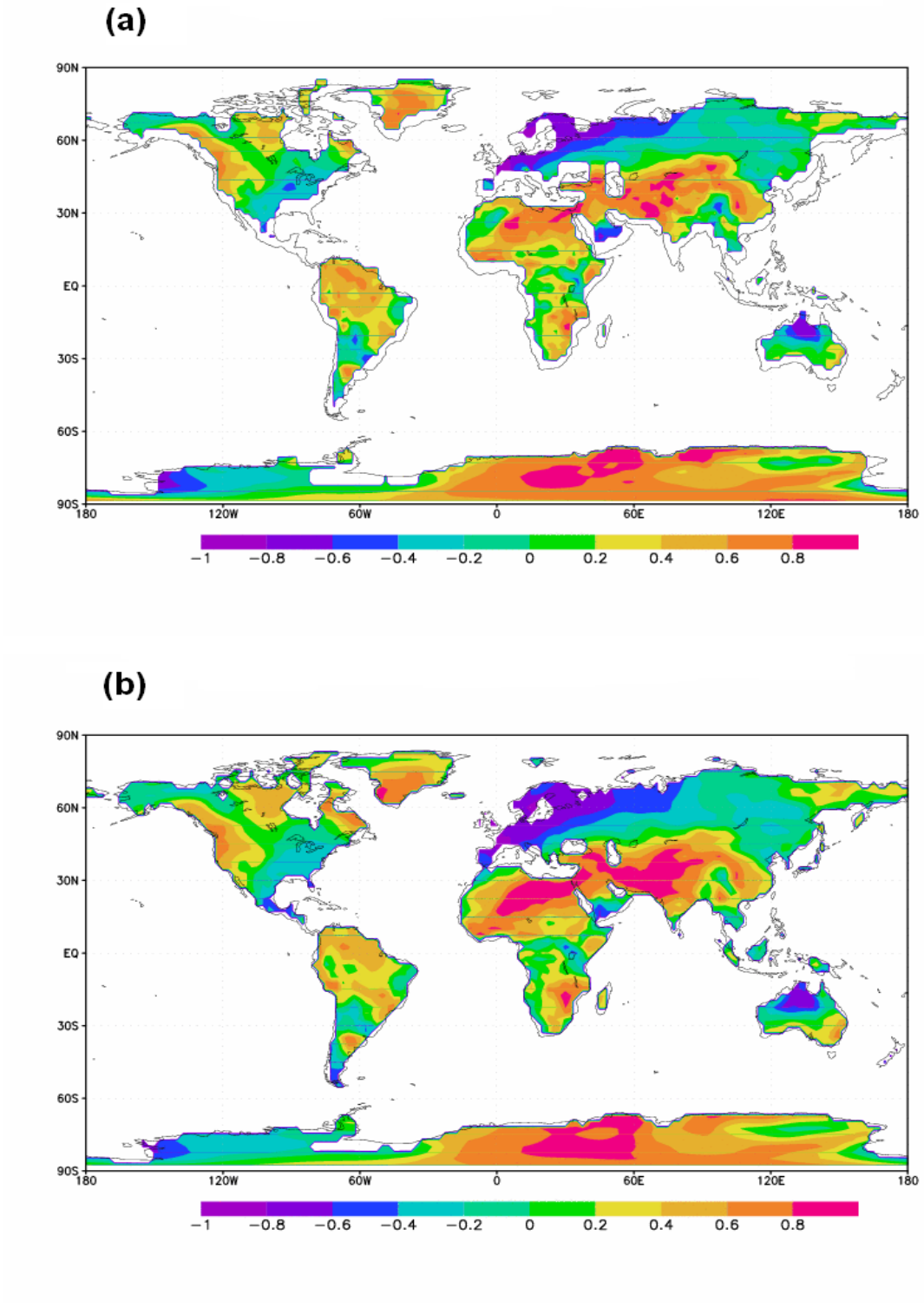

Figure 8: NCEP/NCAR Reanalysis lag correlation coefficients between July Niño 3 SST anomalies and January NCEP/NCAR T_{skin} (192 x 94 grid points) **(a)** + T_{air} (144 x 73 grid points) **(b)** over the period of 2001–2010.

c. Vegetation

Correlation coefficients between Niño 3 SST anomalies and NDVI for January and July show a more complicated pattern than T_{skin} or T_{air}, with greater variability (Figures 9a, 9b). In January, the highest positive correlation coefficient is 0.85, located over northern India (25°N, 75°E). The strongest negative correlation coefficient is -0.79, located in extreme northeastern China near the border of Russia (45°N, 130°E).

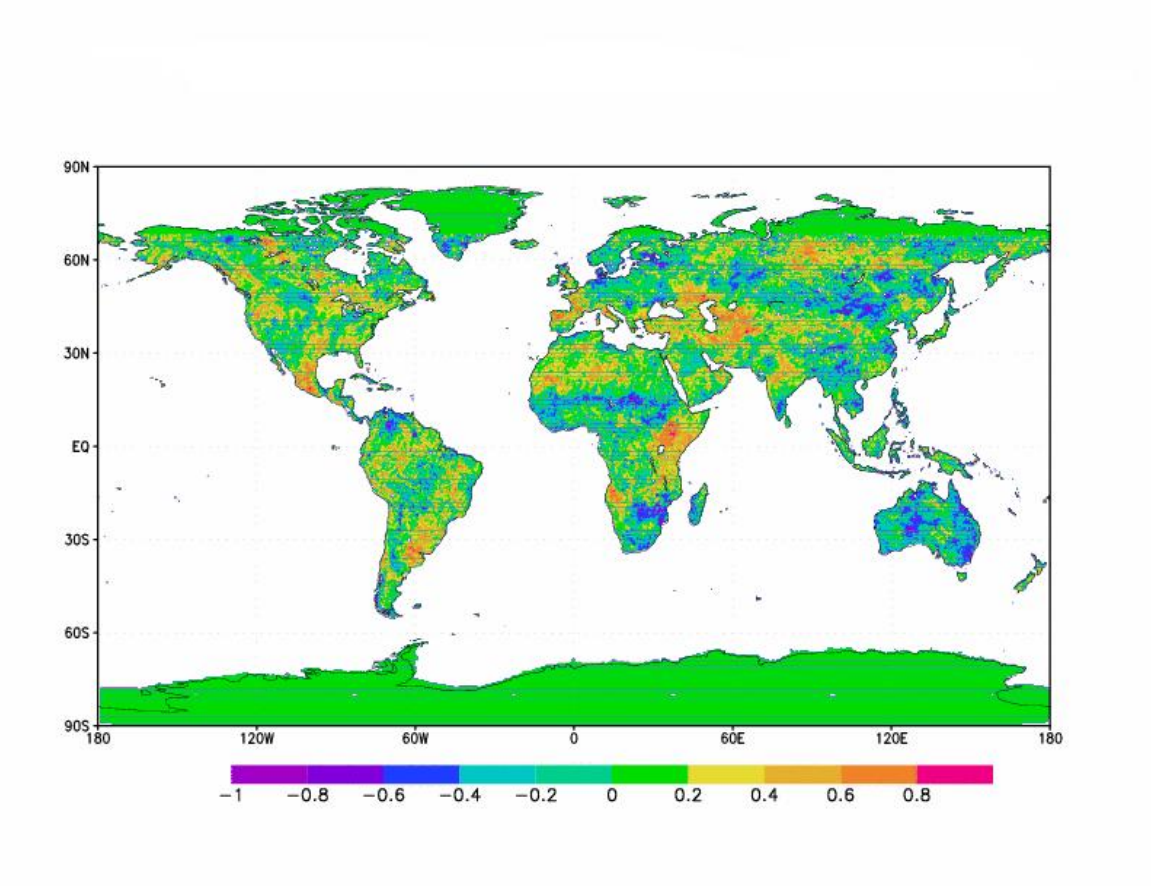

Figure 9a: Correlation coefficients between January Niño 3 SST anomalies and January MODIS NDVI (0.05° x 0.05° resolution, regridded to 0.5° x 0.5°) over the period of 2001–2010.

Over North America, there are generally moderate to strongly positive values (0.4 to 0.8) for the west coast and southern Alaska, similar to the analysis for T_{skin} in January. Parts of the United States east of the Rocky Mountains show strong negative correlation

coefficients (< – 0.6), including in the northern Central Plains, Midwest, and southern Great Lakes regions. There is a large area of weak to strong positive correlation coefficients over northern Mexico (0.2 to 0.8). Northern Africa features a thin latitudinal belt of moderate negative correlations (– 0.4 to – 0.8), but values are generally positive. Conversely, southern Africa has a larger area of weak negative correlation coefficients from 20°S to 40°S. Europe features weak to moderate (0 to 0.6) positive correlations over the western region, with small areas of strongly negative correlation coefficients in the north central region. In Australia, the highest correlations are found in the interior of the content, with slightly negative values along the western and eastern coasts.

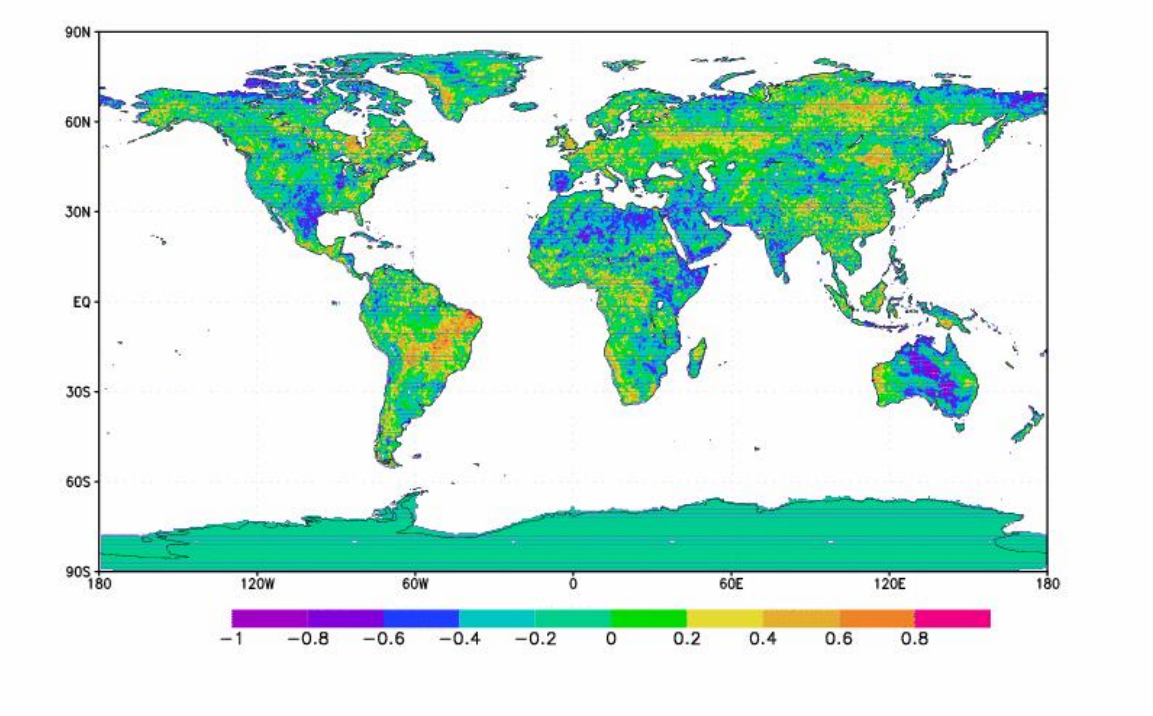

Figure 9b: Correlation coefficients between July Niño 3 SST anomalies and July MODIS NDVI (0.05° x 0.05° resolution, regridded to 0.5° x 0.5°) over the period of 2001–2010.

Nevertheless, the pattern is more complicated than for T_{skin} or T_{air}, with many changes across land areas showing the sensitivity of vegetation. Despite the areas of

strongly positive and negative correlations, the general background trends seem to be values close to zero. A noticeable change between the winter and summer months occurs in the northernmost African countries. In January, positive Niño 3 SST anomalies appear to be associated with higher NDVI values in winter and lower NDVI values in summer in the region between 15°N–30°N.

La Niña results in wetter than normal conditions within southern Africa and drier than normal conditions over equatorial east Africa from December to March (Nicholson and Selato 2000). In January, there are correlation coefficients of – 0.4 to – 1 in southern Africa, which suggests that El Niño conditions should be associated with less vegetation, whereas La Niña events are associated with more greenness of vegetation. More precipitation could lead to a higher NDVI, so there is consistency in this finding. For equatorial east Africa, values are close to zero at the coast but strongly positive further inland (0.2 to 0.8), which suggests that below normal Niño 3 SST anomalies would be associated with less green vegetation possibly due to drier than normal conditions.

The highest positive correlation coefficient for July is 0.86, over the northeastern Brazilian coast (5°S, 40°W). The strongest negative correlation coefficient for July is – 0.84 over central Australia (25°S, 135°E). For North America, the most distinct pattern is an area of moderate to strong negative correlation coefficients (– 0.4 to – 0.8) over the southern United States and northern Mexico, which is opposite of that January. South America features the largest global pattern, with a large area of positive correlations over the northern part of the continent (0.4 to 0.8). Small areas of negative correlation coefficients between – 0.4 and – 0.6 exist throughout northern and eastern Africa, in

particular the Sahara Desert. Finally, opposite the pattern for January, Australia has strong negative correlations in the center of the continent, with the highest values along a thin band on the western coast (0 to 0.8). In general, there are stronger positive relationships between Niño 3 SST anomalies in January than in July.

d. Water Vapor

January correlation coefficients between Niño 3 SST anomalies and PWV (Figure 10a) show similarity to those of Niño 3 SST anomalies and T_{skin} (Figure 3b), especially in the Northern Hemisphere. For example, much of Eurasia has high positive correlation coefficients (0.4 to 0.8), while the Norway/Sweden/Denmark region has very strong negative correlation coefficients (– 0.4 to 1). The pattern over western North America is the same, as is that of Alaska. One difference is over northern Mexico with T_{skin} being negatively correlated and PWV being positively correlated.

An explanation for the similar results is through the relationship between air temperature and potential water vapor: the higher the air temperature, the greater the saturation vapor pressure, as can be shown by the Clausius-Clapeyron relation. However, an increase in the saturation vapor pressure and hence capacity to hold water vapor does not necessarily correspond to an increase in the actual amount of water vapor. Another possible explanation is the greenhouse effect. Higher amounts of PWV enhance the greenhouse effect, resulting in more absorption and re-emission of outgoing infrared radiation, which increases T_{skin}. An important finding is that the patterns are similar in the Northern Hemisphere but not nearly as much in the Southern Hemisphere.

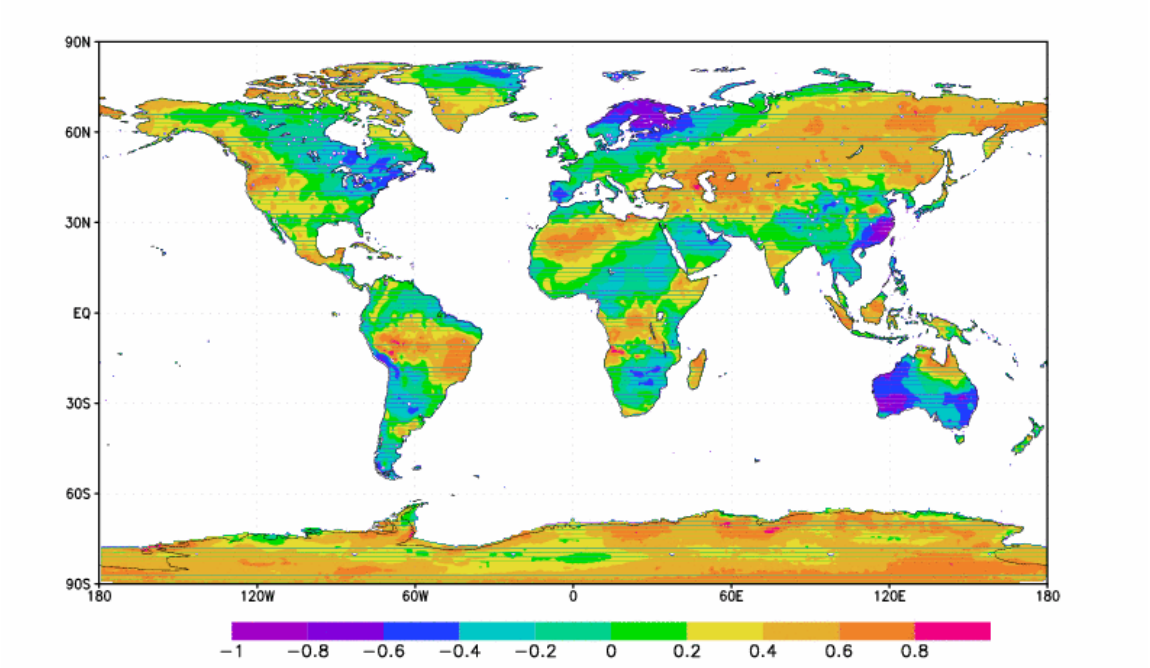

Figure 10a: Correlation coefficients between January Niño 3 SST anomalies and January MODIS PWV over the period of 2001–2010.

The highest correlation coefficient between Niño 3 SST anomalies and PWV for July (Figure 10b) is 0.89, over the northeastern Sahara Desert (30°N, 5°E). The July correlation has similar features to the correlation between Niño 3 SST anomalies and T_{skin} (Figure 3b), but much more substantial differences than for January. First, while most of Australia is covered by weak to strong positive correlation coefficients for T_{skin}, the correlation for PWV features negative correlations over much of the continent. Second, there is a large swath of moderate to strong negative correlations (– 0.4 to – 0.8) extending from northern Alaska southeastward into Canada and the Rocky Mountains of the United States for PWV; this is completely absent for T_{skin}, with very weak correlations over the same area. Finally, while slightly negative correlations exist for T_{skin} over the northeast United States (0 to – 0.4), there are positive values for PWV over

the same region (0.2 to 0.6). Overall, T_{skin} seems more related to PWV in the Northern Hemisphere winter than the summer.

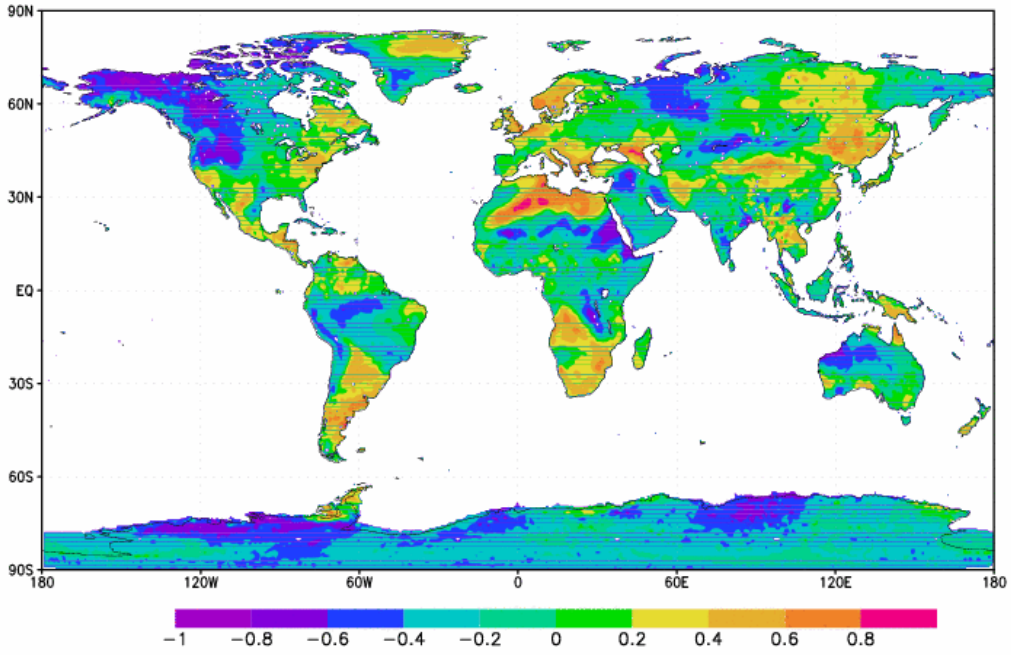

Figure 10b: Correlation coefficients between July Niño 3 SST anomalies and July MODIS PWV over the period of 2001–2010.

A lag correlation analysis comparing January Niño 3 SST anomalies and July PWV (Figure 11a) has a maximum value of 0.86 over the eastern Sahara desert in Africa, (20°N, 30°E) and minimum value of -0.89 over the southern United States (30°N, 105°W). There are several regions with strong negative values (-0.4 to -0.9) including the southwestern Desert and Rocky Mountains in the western United States, southern Africa, a small area in western Australia, an area in middle South America, and two areas in northern Africa. Examining the latitude of these regions, it is found that they are all in

the vicinity of either 30°N or 30°S. As mentioned before, lag correlations for July T_{skin} showed areas of strong negative correlations at these particular latitudes. Despite this similarity, there are many differences between the two variables. For example, for T_{skin} (Figure 4a) slight to strong positive correlations exist in southernmost Africa, which is opposite of that for PWV. The most striking feature is an area of very strong positive correlations over western Canada and Alaska (> 0.8); the only other region with this strong of a relationship is a small area over northeastern Africa (20°N, 30°E).

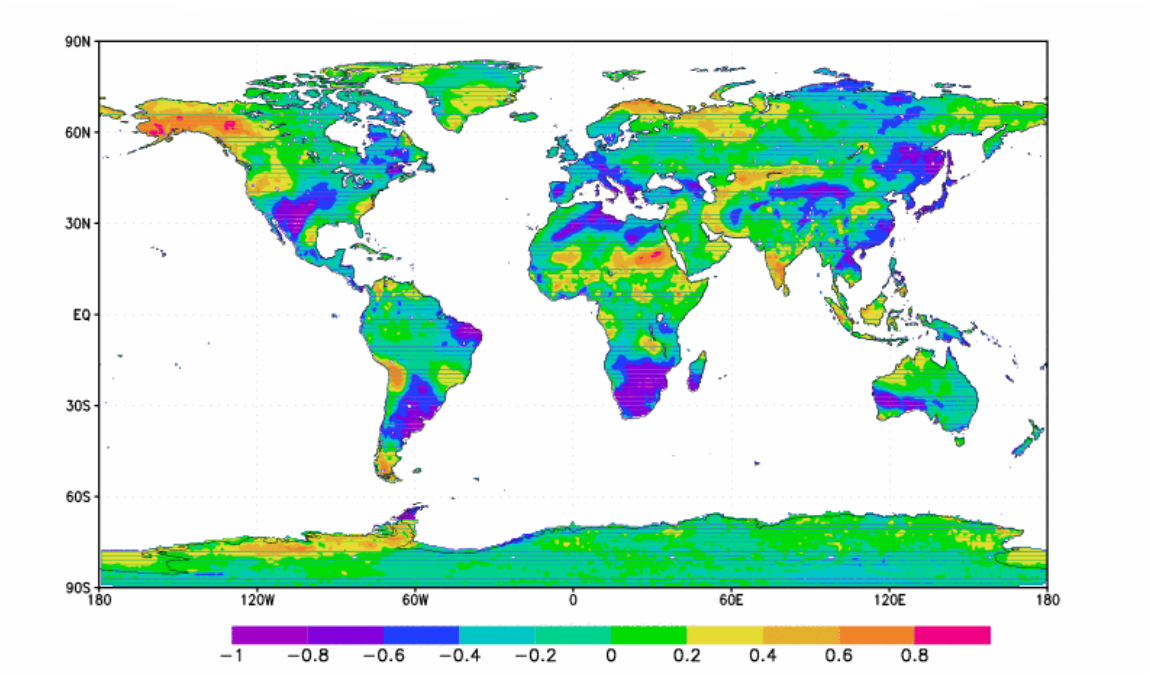

Figure 11a: Correlation coefficients between January Niño 3 SST anomalies and July MODIS PWV over the period of 2001–2010.

The lag correlation of July Niño 3 SST anomalies and January PWV (Figure 11b) has a maximum correlation of 0.95 over southern Alaska (60°N, 150°E) and a minimum correlation of – 0.88 (40°N, 75°E). First, the swath of an almost one-to-one positive relationship over northern Africa is absent for PWV; instead, variable correlations of slightly negative to slightly positive exist over the region. Second, the region of strong

negative values over western and northern Europe is absent as well, with small to moderate positive values over the region (0 to 0.4). Finally, the pattern in Australia shows little resemblance, except for the eastern coast.

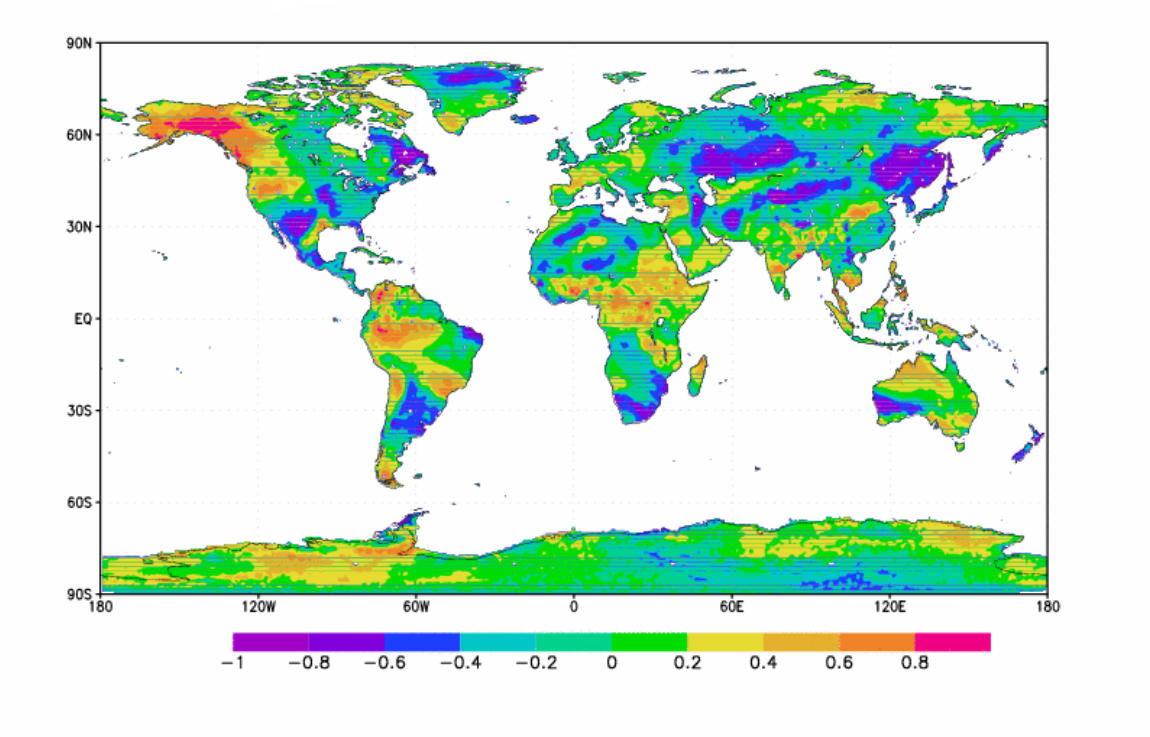

Figure 11b: Correlation coefficients between July Niño 3 SST anomalies and January MODIS PWV over the period of 2001–2010.

4. Uncertainty Analysis

Three major sources of uncertainty remain in this study. The first is related to the satellite data inaccuracies in MODIS T_{skin} retrieval. The second is related to the statistical approach we specifically used. The third is the limits of the NCEP/NCAR Reanalysis Data. Several uncertainties exist for the retrieval of T_{skin} by MODIS. One source of error is cloud contamination (Jin 2004; Jin and Mullens 2012). Never will MODIS have the ability to measure T_{skin} under cloudy skies (Jin and Mullens 2012).

The number of techniques for retrieving T_{skin} from satellite measurements for land applications has greatly increased in recent years**.** MODIS uses thermal infrared bands to measure T_{skin} (Jin and Mullens 2012). It is retrieved from thermal emission at specific wavelengths in which the atmosphere is relatively transparent. However, even in the most transparent regions, atmospheric emissivity and attenuation are not negligible and require correction (Jin 2004; Jin and Dickinson 2010). The split-window algorithm is the primary algorithm used to generate the MODIS T_{skin} products (Wan and Li 1997). It was first suggested in 1970 (Anding and Kauth 1970) as a way to measure T_{skin} by using two separate thermal channels**.** However, this algorithm still has errors in T_{skin} because it is dependent on the infrared wavelength used for the measurement, spectral dependence of the emissivity, angle at which the measurement is made, state of the surface (roughness, surface type, moisture, vegetation cover, etc.), and height of the instrument above the surface (Jin 2000). Overall, there are several factors that can lead to errors in T_{skin} measurement.

T_{skin} is also dependent on land cover (Jin and Dickinson 2010). For instance, a desert surface may heat up more rapidly during the day than a forest. Different land covers produce different levels of emissivity. Hence, errors in emissivity can clearly produce errors in T_{skin}. Also, due to the high land surface heterogeneity, each pixel of the satellite generally contains more than one land type, but MODIS only calculates one T_{skin} value for this pixel (Jin and Mullens 2012). In general, emissivity is one of the largest uncertainty sources in SWT (Jin 2004). T_{skin} will have an error of 0.7°C per 1% emissivity uncertainty (Prata et al. 1995; Jin 2004).

Instrument noise and variability are additional sources of error (Prata et al. 1995). Furthermore, the state of the atmosphere above the surface (i.e., atmospheric moisture distribution, amount, and geometrical distribution of cloud cover and aerosol) also affects the accuracy of T_{skin} measurement. Clearly, there are many sources of uncertainty that can lead to an incorrect T_{skin}. Consequently, a wide range of errors may occur when one tries to measure a single accurate T_{skin} measurement from space (Jin 2004).

Finally, all of the mentioned sources of uncertainty are not independent (Jin 2000). For example, emissivity may vary with viewing angle, so an error in viewing angle could change the value of emissivity, further increasing error of T_{skin}.

Due to the limited duration of data, the statistical approach used may also lead to uncertainty. The Pearson Product-Moment Correlation Coefficient, used in this study, has three key assumptions associated with it (Bachman 2004): (1) the relationship between two variables is linear, (2) both variables constitute interval scales, and (3) both variables are normally distributed. If one or more of these assumptions is not satisfied,

the correlation coefficient may not produce true unbiased relationships between two variables. A normal distribution assumes that half of the data population is below the mean and half is above the mean. In addition, outliers can greatly affect the value of the correlation (Morgan et al. 2010). In a set of data with a clear linear relationship, one data point outside of the main range can greatly distort the strength of the relationship given by the correlation coefficient. It is important to keep all of these assumptions in mind when evaluating the results of this study. More years of data would help increase the degrees of freedom and lower the value of the correlation coefficient required for a level of 95% confidence. However, MODIS Terra data has only been available since 2001, and although ten years of data includes multiple El Niño and La Niña events over the period, it may not be adequate for a serious Pearson Product-Moment analysis.

Finally, the third major area of uncertainty lies in the NCEP/NCAR reanalysis data for T_{air} and T_{skin}. Between 1998–2004, there was disagreement from sea-ice analyses whether a certain location was either ocean or land, particularly in the Arctic region ("NCEP/NCAR Reanalysis Problems List"). This resulted in both T_{air} and T_{skin} being significantly higher than actual values over parts of the polar regions, potentially affecting the values of r.

Also, the NCEP/NCAR reanalysis data has a poor representation of clouds (Trenberth 2004). Clouds have a large effect on the value of T_{skin} (Jin and Dickinson 2010); for example, when a cloud passes over a region, a decrease in T_{skin} occurs due to a decrease in absorbed downward shortwave radiation at the surface. Thus, this particular representation by NCEP/NCAR Reanalysis data could produce errors in T_{skin}.

In addition, soil moisture can cause cooler daytime temperatures through surface evaporation. However, the NCEP/NCAR Reanalysis data omits this important variable. Because of this, along with the poor depiction of clouds, the surface-heat budget has serious errors (Trenberth 2004). Clouds and soil moisture are critical to the surface-heat budget for correct surface temperatures, and hence the reason for inaccuracies. Overall, interpretation of T_{skin} from NCEP/NCAR Reanalysis data is complex (Pepin et. al 2005).

5. Conclusions

This study examines the relationship between ENSO and land surface parameters, both on an instantaneous time scale and lag time scale over the ten-year period of 2001–2010. It shows that many of the relationships between ENSO and air temperature are also found when examining ENSO and skin temperature. In particular, four major results were identified.

First, over North America, air and skin temperature showed warmer than normal values from the northwest region of the United States extending into southern Canada and Alaska for an El Niño event. Cooler January skin temperatures were present over the Gulf States for warmer tropical Pacific temperatures in January that are consistent with the observation that El Niño brings cooler wintertime weather to the Southeast.

Second, cooler January temperatures were associated with a warm ENSO event over central and northern Europe, with the largest cooling being over the Norway/Sweden/Finland region, consistent with past results. However, warmer January conditions existed over much of Siberia, consistent with previous work.

Third, local effects were demonstrated. When January Niño 3 SST anomalies are correlated with MODIS T_{skin} for July, there are positive correlation coefficients (0.4 to 0.8) over the southwest United States including New Mexico, Arizona, and southern portions of Utah and Colorado. However, just to the east is an area of negative correlation coefficients (– 0.4 to – 1) over Texas and Louisiana.

Fourth, the relationships found are likely due to two effects: large scale dynamics, such as cloud cover, rainfall, changes in solar radiation, and circulation, and local mechanisms, including topography and land cover change. ENSO can cause variations in the jet stream, storm tracks, and have a large effect on temperatures, precipitation, vegetation, and water vapor. Changes in tropical atmospheric temperatures have been found to occur one to two seasons after initial variations in ENSO (Newell and Weare 1976; Angell 1981; Pan and Oort 1983; Reid et al. 1989; Yulaeva and Wallace 1994; Kumar and Hoerling 2003). Since similar patterns were found for both MODIS and NCEP/NCAR reanalysis data, as well as for both T_{skin} and T_{air}, there is strong evidence that large scale dynamics could be the cause of how ENSO affects land surface parameters worldwide.

This study is significant because it examines how ENSO affects land surface parameters measured with remote sensing techniques, specifically using MODIS data. Most previous studies have used either observational data or numerical modeling, and so it is important that many of the same patterns are found when ENSO is instead correlated with MODIS variables. In addition, although skin temperature has a different physical meaning than air temperature, along with differences in diurnal and annual cycles, we demonstrated that many of its responses are similar to those of air temperature. Finally, despite the differences in resolution, NCEP/NCAR reanalysis data produces similar correlations for air temperature as MODIS data, although the magnitude of correlations and exact latitudinal and longitudinal extent can vary.

6. Future Work

There are three main areas of future work resulting from this study. First, the time lag between Niño 3 SST anomalies and land surface parameters could be varied. Instead of examining the relationship between the two variables at the same time and six months apart, one could try a shorter lag such as one to three months to see if similar patterns exist. Or, a longer lag could be applied, such as up to one year. Also, it would be interesting to examine different lags for different land surface parameters to account for different response times. For example, vegetation should respond more slowly to a change in Niño 3 than T_{skin}.

Another idea would be to add additional months to the correlations to see changes in patterns and also try to increase levels of significance. For example, if December and February were included for 2001–2010, the degrees of freedom would increase to 28, requiring only a 0.361 correlation for a 95% confidence level. Also, if the variables were averaged over the three month period of December through February, this would keep the degrees of freedom at eight, but allow examination to determine if there are any differences than from January. While Hurrell examined Southern Oscillation responses to El Niño and La Niña events in January (1996), Fraedrich looked at how average December–February temperature anomalies are affected (1994). It is possible that January could have some unique patterns of its own, and using a three-month period instead allows a more representative picture of the average conditions for the key northern hemisphere winter months when the effects of El Niño are strongest.

Finally, a third idea would be to focus on a case study for a particular location, examining the response of multiple surface parameters to El Niño. For example, the high resolution of MODIS would be very helpful to examine the effects of ENSO on Baja deforestation.

References

Anding, D., and R. Kauth, 1970: Estimation of sea surface temperature from space. *Remote Sens. Env.,* **1,** 217-220.

Angell, J. K., 1981: Comparison of variations in atmospheric quantities with sea surface temperature variations in the equatorial eastern Pacific. *Mon. Wea. Rev.,* **109,** 230–242.

Bachman, L. F., 2004: *Statistical analysis for language assessment.* Cambridge University Press, 364 pp.

Becker, F., and Z.L. Li, 1995: Surface temperature and emissivity at various scales: Definition, measurement and related problems. *Remote Sens. Rev.,* **12,** 225-253.

Bjerknes, J., 1966: A possible response of the atmospheric Hadley circulation to equatorial anomalies of ocean temperature. *Tellus,* **18,** 820-829.

Bjerknes, J., 1969: Atmospheric Teleconnections from the Equatorial Pacific. *Mon. Wea. Rev.,* **97,** 163-172.

Coll, C., V. Caselles, J.A. Sobrino, and E. Valor, 1994: On the atmospheric dependence of the split-window equation for land surface temperature. *Int. J. Remote Sens.,* **15,** 105–122.

FCC, 2009: Seasonal Climate Outlook: Winter 2009 [Available at http://climatecenter.fsu.edu/products-services/outlooks/seasonal-climate-outlook-winter-2009]

Fraedrich, K., 1994: An ENSO impact on Europe? *Tellus,* **46,** 541–552.

Hahmann, A.N., and R.E. Dickinson, 2001: A fine-mesh land approach for general circulation models and its impact on regional climate. *J. Climate,* **14**, 1634–1646.

Held, I.M., S. W. Lyons, and S. Nigam, 1989: Transients and the extratropical response to El Niño. *J. Atmos. Sci.,* **46,** 163–174.

Hoerling, M. P., and M. Ting, 1994: Organization of extratropical transients during El Niño. *J. Climate,* **7,** 745–766.

Hoerling, M. P., and A. Kumar, 2000: Understanding and Predicting Extratropical Teleconnections Related to ENSO. Chapter 2 (pp 57-88) in "El Niño and the Southern Oscillation: Multi-scale Variability, and Global and Regional Impacts [eds. H. Diaz and V. Markgraf], Cambridge University Press, 496 pp.

Horel, J., and J. Wallace, 1981: Planetary scale atmospheric phenomena associated with the southern oscillation. *Mon. Wea. Rev.,* **109,** 813-829.

Hoskins, B. J., A. J. Simmons, and D. G. Andrews, 1977: Energy dispersion in a barotropic atmosphere, *Q. J. R. Meteorol. Soc.,* **103,** 553–567.

Hoskins, B. J., and D. J. Karoly, 1981: The steady linear response of aspherical atmosphere to thermal and orographic forcing, *J. Atmos. Sci.,* **38,** 1179–1196.

Hurrell, J., 1996: Influences of variations in extratropical wintertime teleconnections on Northern Hemisphere temperature. *Geo. Res. Let.,* **23,** 665-668.

Ihara, C., Y. Kushnir, M. Cane, and A. Kaplan, 2007: Timing of El Niño-Related Warming and Indian Summer Monsoon Rainfall. *J. Climate,* **21,** 2711-2719.

Jin, M., R.E. Dickinson, and A. M. Vogelmann, 1997: A Comparison of CCM2/BATS Skin Temperature and Surface-Air Temperature with Satellite and Surface Observations. *J. Climate,* **10,** 1505-1524.

Jin, M., and R.E. Dickinson, 1999: Interpolation of surface radiation temperature measured from polar orbiting satellites to a diurnal cycle. Part 1: Without clouds. *J. Geophys. Res.,* **104,** 2105- 2116.

Jin, M., 2000: Interpolation of surface radiation temperature measured from polar orbiting satellites to a diurnal cycle. Part 2: Cloudy-pixel Treatment. *J. Geophys. Res.*, **105**, 4061-4076.

Jin, M., 2004: Analysis of Skin Temperature Variations Using Long-Duration AVHRR Observations. *Bull. Am. Met. Soc.*, **85,** No. 4, 587-600.

Jin, M., and J.M. Shepherd, 2008: Aerosol relationships to warm season clouds and rainfall at monthly scales over east China: Urban land versus ocean. *J. Geophys. Res.*, **113,** D24S90, doi:10.1029/2008JD010276.

Jin, M., and R.E. Dickinson, 2010: Land surface skin temperature climatology: benefitting from the strengths of satellite observations. *Environ. Res. Lett.*, **5,** 044004.

Jin, M., and T. Mullens, 2012: Land-Biosphere-Atmosphere Interactions over Tibetan Plateau from MODIS Observations. *Environ. Res. Lett.*, **7,** 014003.

Kao, H.Y., and Jin-Yi Yu, 2009: Contrasting Eastern-Pacific and Central-Pacific Types of ENSO. *J. Climate*, **22**, 615–632.

Kiladis, G. N., and H. van Loon, 1988: The Southern Oscillation. Part VII: Meteorological anomalies over the Indian and Pacific sectors associated with the extremes of the oscillation. *Mon. Wea. Rev.*, **116,** 120-136.

Kiladis, G.N., and H.F. Diaz, 1989: Global Climatic Anomalies Associated with Extremes in the Southern Oscillation. *J. Climate*, **2,** 1069–1090.

King, M. D., W. P. Menzel, Y. J. Kaufman, D. Tanre, B. C. Gao, S. Platnick, S. A. Ackerman, L. A. Remer, R. Pincus, and P.A. Hubanks, 2003: Cloud and aerosol properties, precipitable water, and profiles of temperature and water vapor from MODIS. *IEEE Trans.Geosci.Remote Sens. Lett.*, **41,** 442-458.

Kok, C. J., and J. D. Opsteegh, 1985: Possible causes of anomalies in seasonal mean circulation patterns during the 1982–83 El Niño event. *J. Atmos. Sci.*, **42,** 677-694.

Kumar, A., and M.P. Hoerling, 2003: The Nature and Causes for the Delayed Atmospheric Response to El Niño. *J. Climate*, **16,** 1391-1403.

McPhaden, M. J., 2002: El Niño and La Niña: Causes and global consequences. *Encyclopedia of Global Environmental Change,* T. Munn, Ed., Vol. 1, John Wiley and Sons, 353–370.

Morgan, G. A., N. L. Leech, G. W. Gloeckner, and K. C. Barrett, 2010: *IBM SPSS for Introductory Statistics: Use and Interpretation.* Routledge Press, 243 pp.

Namias, J., 1963: Interactions of Circulation and Weather between Hemispheres. *Mon. Wea. Rev.,* **91,** 482-486.

Namias, J., 1976: Some Statistical and Synoptic Characteristics Associated with El Niño. *J. Phys. Oceanogr.,* **6,** 130-138.

Newell, R. E., and B.C. Weare, 1976: Factors governing tropospheric mean temperature. *Science,* **194,** 1413–1414.

Nicholson, S.E., and J.C. Selato, 2000: The influence of La Niña on African rainfall. *Int. J. Climatol.* **20,** 1761-1776.

Pan, Y. H., and A. H. Oort, 1983: Global climate variations connected with sea surface temperature anomalies in the eastern equatorial Pacific Ocean for the 1958–73 period. *Mon. Wea. Rev.,* **111,** 1244–1258.

Pepin, N. C., M. Losleben, M. Hartman, and K. Chowanski, 2005: A comparison of SNOTEL and GHCN/CRU surface temperatures with free-air temperatures at high elevations in the western United States: Data compatibility and trends. *J. Climate,* **18,** 1967–1985.

Prata, A. J., V. Caselles, C. Colland, J. A. Sobrino, and C. Ottle, 1995: Thermal remote sensing of land surface temperature from satellites: Current status and future prospects. *Remote Sens. Rev.,* **12,** 175–224.

Rasmusson, E. M., and T. H. Carpenter, 1982: Variations in sea surface temperature and surface wind fields associated with the Southern Oscillation/El Niño. *Mon. Wea. Rev.,* **110,** 354-384.

Rasmussen, E.M., R.E. Dickinson, J.E. Kutzbach, and M.K. Cleaveland, 1993: Climatology. *Handbook of Hydrology*, D. Maidment, Ed., McGraw-Hill.

Reason, C. J. C., and D. Jagadheesha, 2005: Relationships between South Atlantic SST Variability and Atmospheric Circulation over the South African Region during Austral Winter. *J. Climate*, **18**, 3339–3355.

Reid, G. C., K. S. Gage, and J. R. McAfee, 1989: The thermal response of the tropical atmosphere to variations in equatorial Pacific sea-surface temperatures. *J. Geophys. Res.,* **94,** 14 705–716.

Ricard, J.P., 2000: Regional impacts of El Niño on Europe and the Mediterranean Basin (bilingual - French title: Impacts régionaux de El Niño sur l'Europe et le bassin Méditerranéen). MEDIAS newsletter (bilingual: la lettre de MEDIAS), **12,** 27-29.

Ropelewski, C.F., and M.S. Halpert, 1986: North American Precipitation and Temperature Patterns Associated with the El Niño/Southern Oscillation (ENSO). *Mon. Wea. Rev.,* **114,** 2352-2362.

Ropelewski, C. F., and M. S. Halpert, 1987: Global and regional scale precipitation patterns associated with the El Nino/ Southern Oscillation. *Mon. Wea. Rev.,* **115,** 1606-1626.

Schaaf, C. B., F. Gao, A. Strahler, W. Lucht, X. Li, T. Tsang, N.C. Strugnell, X. Zhang, Y. Jin, J. P. Muller, P. Lewis, M. Barnsley, P. Hobson, M. Disney, G. Roberts, M. Dunderdale, C. Doll, R.P. d'Entremont, B. Hu, S. Liang, J. L. Privette, and D. Roy, 2002: First operational BRDF, albedo, nadir reflectance products from MODIS, *Rem. Sens. Env.,* **83,** 135-148.

Schneider, E. K., M. Fan, B. P. Kirtman, and P. A. Dirmeyer, 2006: Potential effects of Amazon deforestation on tropical climate. IGES/COLA Rep., 41 pp.

Shem, W.O., and R.E. Dickinson, 2006: How the Congo Basin deforestation and the equatorial monsoonal circulation influences the regional hydrological cycle. Paper presented at the 86th Annual AMS Meeting, January 2006.

Simmons, A.J., J.M. Wallace, and G. Branstator, 1983: Barotropic wave propogation and instability and atmospheric teleconnection patterns. *J. Atmos. Sci.*, **40,** 1363-1392.

Sittel, M.C., 1994a: Marginal probabilities of the extremes of ENSO events for temperature and precipitation in the southeastern United States. Tech. Rep. 94-1, Center for Ocean-Atmospheric Prediction Studies, 155 pp. [Available from COAPS, Tallahassee, FL 32306-2840.]

Sittel, M.C., 1994b: Differences in the means of ENSO extremes for maximum temperature and precipitation in the United States. Tech. Rep. 94-2, Center for Ocean-Atmospheric Prediction Studies, 50 pp. [Available from COAPS, Tallahassee, FL 32306-2840.]

Trenberth, K.E., 1984: Signal versus Noise in the Southern Oscillation. *Mon. Wea. Rev.*, **112,** 326-332.

Trenberth, K.E., and T.J. Hoar, 1996a: The 1990-1995 El Niño-Southern Oscillation event: Longest on record. *Geo. Res. Let.*, **23,** 57-60.

Trenberth, K. E., and T. J. Hoar, 1996b: The 1990-1995 El Niño-Southern Oscillation event: Longest on record. Proc. Symposium on Global Ocean-Atmosphere-Land System (GOALS). Atlanta, 28 January-2 February 1996, 84-87.

Trenberth, K. E., 1997: The definition of El Niño. *Bull. Amer. Met. Soc.*, **78,** 2771-2777.

Trenberth, K. E., 2004: Rural land-use change and climate. *Nature*, **427,** 213.

Wallace, J. M., and D. S. Gutzler, 1981: Teleconnections in the geopotential height field during the Northern Hemisphere winter. *Mon. Wea. Rev.*, **109**, 784-812.

Wan, Z., and J. Dozier, 1996: A generalized split-window algorithm for retrieving land surface temperature from space. *IEEE Trans.Geosci.Remote Sens. Lett.*, **34**, 892–904.

Wan, Z., and Z.L. Li, 1997: A physics-based algorithm for retrieving land-surface emissivity and temperature from EOS/MODIS data. *IEEE Trans. Geoscience and Remote Sensing*, **35,** 980-996.

Wan, Z, 2006: MODIS land surface temperature products user's guide. Institute for Computational Earth System Science, University of California, Santa Barbara, CA.

Wang, H. and R. Fu, 2000: Winter Monthly Mean Atmospheric Anomalies over the North Pacific and North America Associated with El Niño SSTs. *J. Climate*, **13,** 3435-3447.

Wilby, R., 1993: Evidence of ENSO in the synoptic climate of the British Isles since 1880, *Weather*, **48,** 234–239.

Wyrtki, K., 1975: El Niño—The Dynamic Response of the Equatorial Pacific Ocean to Atmospheric Forcing. *J. Phys. Oceanogr.*, **5**, 572–584.

Yarnal B., and H. F. Diaz, 1986: Relationships between extremes of the southern oscillation and the winter climate of the Anglo-American Pacific coast. *J. Climate*, **6,** 197-219.

Yulaeva, E., and J. M. Wallace, 1994: The signature of ENSO in global temperature and precipitation fields derived from microwave sounding unit. *J. Climate*, **7,** 1719-1736.

Zeng, N., R. E. Dickinson, and X. Zeng, 1996: Climatic impact of Amazon deforestation—a mechanistic model study. *J. Climate*, **9**, 859-883.

APPENDIX: ACRONYMS

ENSO	El-Nino Southern Oscillation
MODIS	Moderate Resolution Imaging Spectroradiometer
NDVI	Normalized Difference Vegetation Index
PWV	Precipitable Water Vapor
SD	Standard Deviation
SO	Southern Oscillation
SST	Sea-Surface Temperature
T_{air}	Air Temperature
T_{skin}	Skin Temperature